Theses and Dissertations

Fall 2010

# Segmentation of lung tissue in CT images with disease and pathology

Panfang Hua
*University of Iowa*

Recommended Citation

Hua, Panfang. "Segmentation of lung tissue in CT images with disease and pathology." MS (Master of Science) thesis, University of Iowa, 2010.
http://ir.uiowa.edu/etd/819.

www.manaraa.com

SEGMENTATION OF LUNG TISSUE

IN CT IMAGES WITH DISEASE AND PATHOLOGY

by

Panfang Hua

A thesis submitted in partial fulfillment of the
requirements for the Master of Science
degree in Biomedical Engineering
in the Graduate College of
The University of Iowa

December 2010

Thesis Supervisor: Professor Joseph M. Reinhardt

Graduate College
The University of Iowa
Iowa City, Iowa

CERTIFICATE OF APPROVAL

————————————————————

MASTER'S THESIS

—————————————

This is to certify that the Master's thesis of

Panfang Hua

has been approved by the Examining Committee for the thesis requirement for the Master of Science degree in Biomedical Engineering at the December 2010 graduation.

Thesis Committee: ——————————————————————
Joseph M. Reinhardt, Thesis Supervisor

——————————————————————
Eric A. Hoffman

——————————————————————
Edwin L. Dove

# ACKNOWLEDGEMENTS

First of all, I would like to thank my parents and grandparents for their selfless love. Without their support, I would never had the chance to get in touch with the state-of-the-art research, meet the leading scientists in the world and study here at the University of Iowa.

I wish to express my sincere gratitude to Prof. Joseph M. Reinhardt for his precious advice, guidance and support throughout my study. I am greatly indebted to him for his confidence in me, his inspiring and encouraging words and his wealth of brilliant ideas during the research. He is the best advisor that I have ever seen. I would like to thank Prof. Eric A. Hoffman for his support and advice in CT imaging and data analysis. I aslo thank to Prof. Edwin L. Dove for his great advice on the thesis. I appreciate Dr. Kai Ding who give me valued ideas and endless help during my master degree study. I am grateful to Qi Song, without his guidance on graph search algorithm I could not finish the work smoothly. I appreciate Dr. Zhiyun Gao and Kunlin Cao for their help on rib detection and registration. My special thanks go to Janice Cook-Granroth for providing the lung manual segmentation. I would also like to thank Prof. Milan Sonka and his student Dr. Yin Yin for their enlightening talks on graph search algorithm. Thanks to my labmates Kai Ding, Xiayu Xu, Weichen Gao, Kaifang Du, Tarunashree Yavarna, Vinayaka and Sudarshan Bommu for their help and friendship.

The contributions of all these people are greatly appreciated.

# ABSTRACT

Lung segmentation is an important first step for quantitative lung CT image analysis and computer aided diagnosis. However, accurate and automated lung CT image segmentation may be made difficult by the presence of the abnormalities. Since many lung diseases change tissue density, resulting in intensity changes in the CT image data, intensity-only segmentation algorithms will not work for most pathological lung cases. This thesis presents two automatic algorithm for segmentation of pathological lung. One is based on the geodesic active contour, another method uses a graph search driven by a cost function combining the intensity, gradient, boundary smoothness, and the rib information. The methods were tested on several 3D thorax CT data sets with lung disease. Given the manual segmentation result as gold standard, we validate our methods by comparing our automatic segmentation results with Hu's method. Sensitivity, specificity, and Hausdorff distance were calculated to evaluate the methods.

# TABLE OF CONTENTS

# LIST OF TABLES

# LIST OF FIGURES

# CHAPTER 1
# INTRODUCTION

## 1.1   Motivation

Segmentation refers to the process of finding the boundary of the objects in the image. Why do we need to do lung segmentation in computed tomography (CT) images? Lung segmentation is very important since it is the first step for further quantitative lung analysis in computer aided diagnosis, such as lung volume measurement, texture analysis for certain diseases detection. An accurate lung segmentation result is required in order to detect the abnormalities in the next step. For example, it is unlikely to detect a nodule if the nodule is failed to be segmented as lung tissue in the first segmentation step.

After understanding the significance of the lung segmentation, then how can we segment the lung in the CT images? Undoubtedly, manual segmentation is one of the solutions. Humans are very smart, technologists could use lots of underlying information and their knowledge to get an accurate segmentation result. However, it takes a well trained technologist around 36 seconds to trace the lungs boundary on one slice (512*512 pixels), so 5 hours to finish one 500 slices CT image. Moreover, according to the 2007 New England Journal of Medicine study, 19.2 million lung CT was done every year. And most of the CT data sets have a size range from $512*512*450$ to $512*512*600$ according to the respiratory phase. Thus, with the advancement of the CT facilities and the overwhelming number of CT data sets produced every year, manual segmentation is obviously not a practical solution since it is time-consuming and requires lots of tedious work. Hence, semi-automatic segmentation methods

[13, 14] appeared, speeded up the whole segmentation process and saved radiologists from repetitive work. But it still needs some manual interaction. Thanks to the continuous efforts that the image processing genius made to the lung segmentation field, a large number of automatic lung segmentation algorithms [12, 35, 2, 5, 17, 30] are proposed.

However, accurate and automated lung segmentation in CT images is highly challenged by the presence of the abnormalities. Since lung diseases will change the tissue density which will cause the gray level changes in CT images, gray level based lung segmentation algorithms [12, 35, 2, 5] will not work for most pathological lung cases (Fig 1.1). Although many other methods [23, 26, 31, 22, 1, 8, 32] are suggested to segment pathological lung CT images, finding an efficient, robust and accurate automatic pathological lung segmentation algorithm is still an unsolved problem.

## 1.2   Background

### 1.2.1   Lung Imaging

#### 1.2.1.1   Radiography

X-ray is an electromagnetic ray discovered by Wilhelm Conrad Roentgen in 1895. X-rays have an energy in the range of 0.12 kev to 120 keV and a wavelength in range of 10 to 0.010 nm. X-rays are generated in an X-ray tube where the electrons released from a cathode are accelerated by the high voltage, and then collide with the anode target. During the collision, two different atomic processes happen: bremsstrahlung and x-ray fluorescence. A continuous spectrum of X-rays is created by bremsstrahlung when the electrons are scattered by the strong electric field near the nuclei. Distinctive frequency X-ray photons are emitted when the electron have
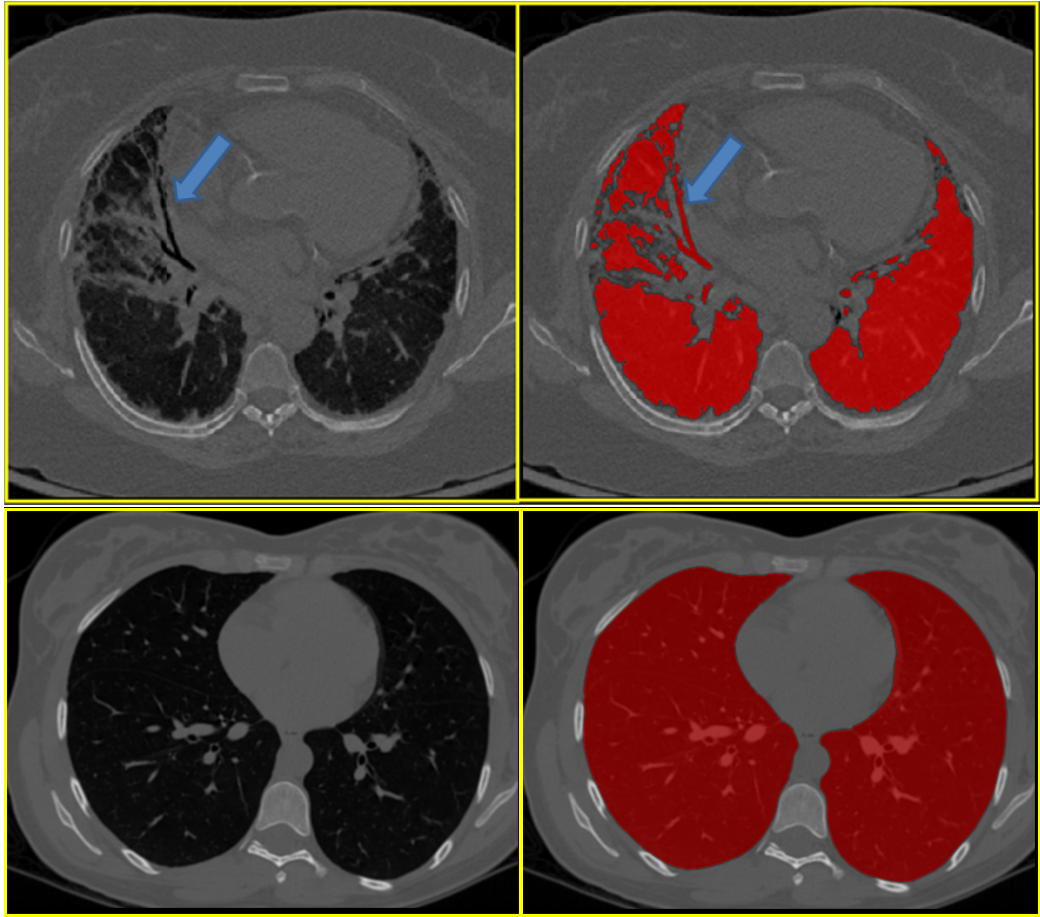
Figure 1.1: Examples of lung CT images. From left to right: transverse view image, transverse view image overlapped with intensity-based lung segmentation algorithm result(red mask). First row: pathological lung CT data set; second row: normal lung CT data set. An example of pathological lung region is pointed by the blue arrows which make the segmentation difficult.

enough energy to knock out an orbital electron, and higher-energy-level electrons fill up the vacancy.

Radiography is an imaging technique that is widely used in medical, security, non-destructive testing, archeology and food inspection. It uses X-rays to allow imaging of the internal features. X-rays are projected to the object, and then absorbed more or less when crossing the object, finally the remaining X-rays are captured by the detector or the X-ray sensitive film to form the 2D image. In the chest X-ray image, bones are always brighter than the soft tissue because compared with the soft tissue, bones have a higher calcium, potassium, magnesium, and phosphorus percentage which will result in a higher electron density and a larger attenuation coefficient.

2-D chest radiography is a type of radiography used to diagnose the conditions of organs in the chest area, such as emphysema, lung cancer and pneumonia. However, interpretation of images is highly challenged by the superposition of the anatomical structures. Thus, for some diseases, chest radiography is good for screening but not for diagnosis. To overcome this disadvantage, computed tomography was invented to obtain a cross-sectioned image.

### 1.2.1.2 X-ray Computed Tomography

Computed tomography is a medical imaging technique invented by Godfrey Hounsfield and Allan McLeod Cormack in 1972 based on the Radon transform. The basic principle behind CT is that the two-dimensional internal structure of an object can be reconstructed from a series of one-dimensional "projections" of the object acquired at different angles. The intensities of these projection signals are dictated by a two-dimensional distribution of tissue attenuation coefficients within the slice.

Multiple two-dimensional X-ray image slices are acquired to reconstruct the 3D volume CT image. Each pixel value of CT image represents the X-ray mass attenuation coefficient or the tissue electron density at each position.

Why is CT so popular in the lung imaging field? CT employs ionizing radiation X-ray which may cause DNA damage and an increased lifetime risk of cancer. Hence, CT is not recommended for children and pregnant women unless it is necessary. Moreover, the main issue within radiology today is to find a good balance between controlling dose and obtaining enough information for reliable diagnosis. However, CT is faster, less sensitive to patient movement and can be still performed for persons with implanted medical devices. Hence, CT is a more appropriate imaging method for motional organs, such as lungs. Meanwhile, magnetic resonance imaging (MRI) is noninvasive and gives a more clear and detailed image of soft tissue, such as brains, internal pelvic organs, knees or shoulders. In addition, ultrasound imaging technology is safe and real-time, thus it is widely used to visualize muscles, tendons, and many internal organs in order to measure their size, structure and abnormalities.

A chest CT scan acquired by state-of-the-art CT scanners usually has isotropic resolution of around 0.5 mm. Generally, it contains over 400 slices, where each slice has a size of 512 by 512 pixels. For detailed description of CT and its application [25] is a valuable source. Fig1.2 shows the three different views of a chest CT scan.

### 1.2.2 Pulmonary Anatomy

Lungs are the major organ of the respiratory system (Fig 1.3). They take a major role in oxygen and carbon dioxide exchange between an organism and the external world. There are two lungs, the left and the right. Left lung is further
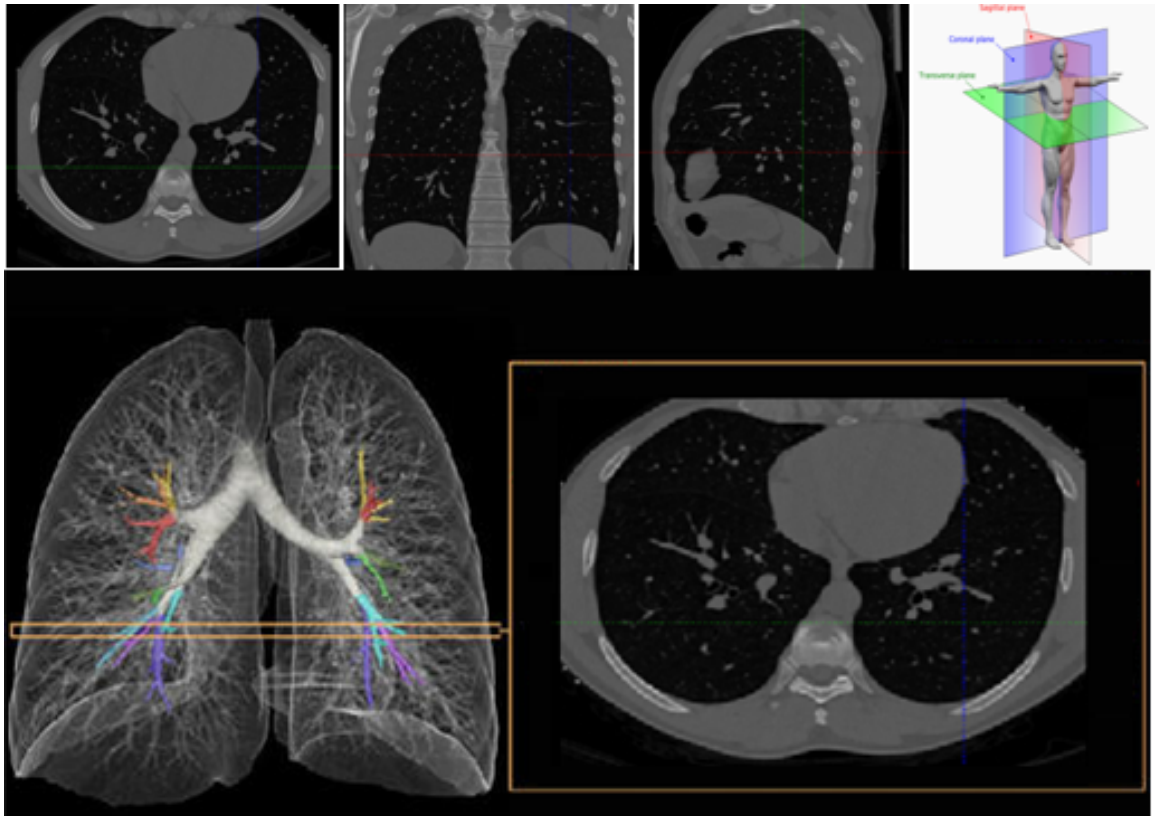
Figure 1.2: Example of a chest CT scan

* Source: First row(from left to right): the transverse view, the coronal view, the sagittal view, the 3D human anatomy planes which is from {33}; the second row(from left to right): 3D rendering of the lung anatomy, transverse view slice.

divided into two lobes, the upper and the lower one, while right lung is divided into three lobes, the upper, the middle and the lower lobes. The airway starts from the trachea, and then divides into the two bronchi, each enters one lung. Within the lung, the airway further divides in to narrower and shorter tubes, and finally connect to the alveoli, the air-containing sacs. Parenchyma is the essential tissue of the lung which includes bronchioles, bronchi, blood vessels, interstitium, and alveoli.
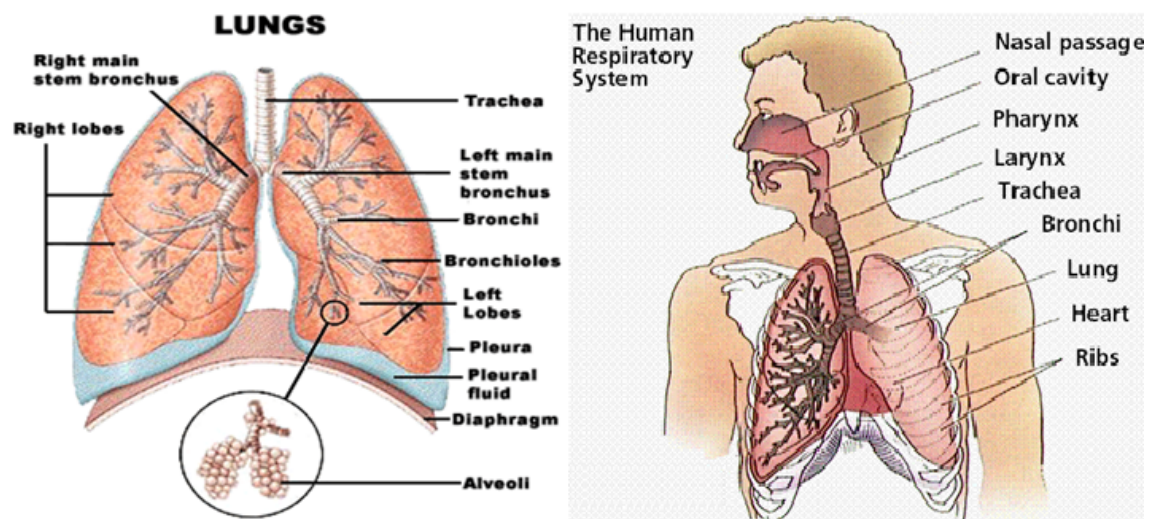


Figure 1.3: the pulmonary anatomy.

* Source: The left figure is from {9}, and the right figure is from {10}

Human rib cage consists of 24 ribs, the thoracic vertebrae, the sternum, and the costal cartilages. Covered by the pleura and then the rib cage, the left and the right lungs are separated by the heart and mediastinum within the ribcage. The apex of each lung extends up to the lowest part of the neck, while the bottom of each lung extends down to the diaphragm. During the inhalation, the expansion of the rib cage and the flatten of the diaphragm cause the the airway sub-atmospheric pressure and

the influx from the environment into the lung. During the exhalation, the relax of the rib cage and the diaphragm cause the recoil of the rib cage and the influx from the lung to the environment. Hence, the rib cage and the lung outer boundary is always very close in all lung respiratory phases.

### 1.2.3  Lung Disease

The term lung disease Fig 1.1 refers to the any disorder or disease that occurs in the lungs or that causes the lungs to not work properly. Generally, lung diseases are divided into three categories: 1) lung tissue disease, such as pulmonary fibrosis, lung cancer and sarcoidosis; 2) airway disease, for example, asthma, emphysema, and chronic bronchitis; 3) Pulmonary circulation diseases, such as blood vessel inflammation. Actually most lung diseases involve a combination of these categories.

According to the latest report  [24] by the American Lung Association, lung disease is the third leading cause of death in the United States, taking around 40 million American lives every year. Lung disease and other lung infections and illnesses are the number one killer of infants. The precise cause of many lung diseases is still unknown.  But the widely known influence factors includes smoking, air pollution, radon gas, and asbestos.

Pulmonary function tests use a spirometer to measure the amount and the speed of air that a subject can breathe in and out during a pre-determined period of time. Pulmonary function tests are useful and harmless diagnostic tools for early disease detection, such as asthma, bronchitis, cystic fibrosis, and emphysema.  In addition, chest X-ray, CT, bronchoscopy, biopsy of the lung or pleura, and ventilation - perfusion scan are also widely used to detect lung diseases.

## 1.3    Previous Work

The first articles about computer analysis of 2D chest X-ray radiography appeared in the 1960s [4, 20]. Becker's group employed computers to perform automatic lung diagnosis. Since then many approaches have been proposed to segment lung automatically in 3D thorax CT images. And lung segmentation algorithms could be divided into several categories: (1)intensity-based method, (2)statistical approach, (3)registration-based method, (4)anatomical knowledge based approach, (5) other innovative methods.

Since lungs contain a significant volume of air and lung tissues appear dark in the CT images (Fig 1.2), conventional lung segmentation algorithms [12, 35, 2, 5] based on the gray level are the most common and straight forward method. For example, Hu et al. presented a threshold-based region-filling algorithm to segment the lung region [12]. Zheng et al. proposed a 3D thresholding method based on histogram characteristics [35]. Although conventional lung segmentation algorithms are simple and quick, they may fail to deal with the low contrast cases, such as pathological lung cases with cystic fibrosis.

Statistical models have been applied to obtain the lung boundary. For example, Li et al. obtained a 3-D active shape model based on the training data sets and treat it as an initial segmentation, then the result is refined according to the fine details and shape variance captured by snake [17]. Van Ginneken et al. [30] proposed an active shape model followed by a KNN classifier as a refinement process. These statistical methods always require a large number of training data and are computational expensive. Moreover, in order to deal with the pathological lung segmentation El-BaZ et al. [1, 8] proposed a new stochastic framework for accurate lung segmenta-

tion. The stochastic framework contains two probabilistic models:a linear combined Gaussian model is used to estimate the image intensity, while the Markov Gibbs random field is used to model the spatial interaction of the neighborhood pixels. Based on these two models, El-BaZ et al. [1] convert the segmentation problem into a min cut graph problem. Thus, the final segmentation result is the optimized solution that minimize the energy function. This novel approach does better with the abnormal lung tissue than intensity-based algorithms. Based on the same two models, Ayman and El-BaZ et al. [8] also tried to use expectation maximization algorithm followed by iterative refinement to obtain the lung region. This algorithm works better in low dose CT image than iterative thresholding method, although there are still small errors near the boundary.

Sluimer et al. showed a refined registration based segmentation approach. It registers a probabilistic atlas to target image to obtain initial segmentation, and then use KNN classifier to refine the boundary based on image features [26]. This method has a significant improvement in segmentation accuracy compared to a standard segmentation-by-registration approach and it can deal with most pathological cases. However, it is very time-consuming due to the CT image registration and classification processes. Van Rikxoort et al. improved this method by adding an error detection step so that refined registration based segmentation method is only implemented if conventional lung segmentation algorithm fails [31].

Anatomical knowledge based method uses other anatomical structures information to obtain the segmentation result. For example, in 1999 Brown et al. proposed a knowledge based lung segmentation method [6]. The key components of the segmentation system is the anatomical model, the inference engine and image processing

routines. Segmentation process is deduced to matching the extracted objects from the image to the objects in the model. Later, Prasad et al. [22] proposed using rib curvature to help the lung segmentation result. This method can obtain more accurate segmentation than iterative thresholding for pathological lung cases, but 2D ribs curvature information cannot well define the lung apex and lung base region.

Large number of other innovative lung segmentation methods have been suggested. Pu et al. [23] suggested an adaptive border marching approach to robustly correct missed juxtapleural nodules while minimizing under-segmentation and over-segmentation relative to the true lung border. However, it may fail to include areas in the lung affected by interstitial disease because these areas missed in the initial segmentation step are so large that convex shape information could not help. Wang et al. reported a texture analysis-based method for accurate severe interstitial disease lung segmentation [32]. And many other image segmentation algorithms are applied to segmentation the lung in the CT image, such as watershed algorithm [16], wavelet transform [29].

Meanwhile, graph based segmentation method becomes more and more popular these days. Li et al. [18] proposed a graph search based framework to obtain globally optimal surface which was widely employed to segment 3D objects in medical images, such as airway, vascular wall layer, bone and cartilage, bladder, and prostate. Yin et al. suggested to use electric field direction lines for graph column construction, and this method was applied to bone and cartilage segmentation [34]. Garvin et al. proposed a graph search method that combined region information into the cost function, and this method was applied to the intraretinal layers segmentation of macular optical coherence tomography images [11]. Song et al. suggested to combine the

prior shape information into the graph arc weight, and the new graph search method was applied to segment the bladder and prostate [27].

## 1.4 Our Work

Although a few algorithms have been also suggested to deal with pathological lung segmentation in volumetric CT images, such as the registration based method, the rib curvature based approach, the texture analysis based method, novel stochastic model based approach and the adaptive border marching method, they are either time consuming or only fit for certain kind of disease lungs.

Our work proposed two methods to deal with the pathological lung segmentation: geodesic active contour based pathological lung segmentation in section 2.2 and graph search based lung segmentation in section 2.3. Then we compared the results of three methods (Hu's method, geodesic active contour based method, and graph search based method) in chapter 3 and chapter 4.

For the geodesic active contour based method, a standard anatomical model (atlas) is constructed by calculating the probability map from the registration result of ten normal segmented lungs and ribcages. This approach is consisted of four steps. Firstly, iterative threshold based region growing algorithm followed by a dilation is used to obtain the initial lung segmentation. Secondly, after identification of the ribcage by thresholding, inter-subject registration between the ribcage in the model and the ribcage of the target image is applied to obtain a transformation matrix, then based on the transformation matrix the lung probability map of the standard anatomical model is warped to the target image to obtain a region of interest probability map. Thirdly, by combining the gradient information, probability map and

other anatomical structures location information, speed image is obtained for the geodesic active contour method. Finally, geodesic active contour is applied to shrink the initial lung segmentation to the true boundary according to the speed image.

For the graph search based lung segmentation method, the aim of our work is to adjust the graph search algorithm to automatically segment severe pathological lung from CT images. The framework is consisted by three steps. The first step is the conventional intensity based lung segmentation to obtain an initial segmentation. The second step is other anatomical structures detection. The third step is combining gray level, boundary smoothness, anatomical information, as well as gradient to refine the lung segmentation result.

# CHAPTER 2
# METHODS

## 2.1 Overview of the Method

As mentioned in chapter 1, lung segmentation is the first step for computer-aided diagnosis. An accurate lung segmentation is prerequisite for further quantitative analysis and abnormal tissue detection. However, automatic lung segmentation in CT images is highly challenged by the presence of the abnormally dense tissue. Our work tries to solve this problem by developing an automatic pathological lung segmentation approach.

Our work is an extension of Hu's Method [12]. Our approaches combines intensity, anatomical information, and gradient to obtain the accurate lung mask. Since the rib cage and the outer lung boundary are very close, rib cage information could guide the lung segmentation process.

Geodesic active contour based method consists of four stages (Figure 2.1):

(1) lung pre-segmentation: optimal thresholding is applied to obtain the lung mask, dynamic programming is used to separate the left lung and the right lung ; This step is similar to Hu's method work;

(2) atlas-based registration: a rib and lung atlas is constructed, inter-subject rib cage registration is employed to map the standard lung probability atlas to the target CT image to obtain a lung region probability map;

(3) Boundary adjustment: geodesic active contour is applied to combine the smoothness, the lung shape information, the gradient information, and the anatomical rib cage information to obtain the left and the right lung regions;

(4) Post processing: the largest component analysis and opening is employed to obtain the final result.

Graph search based method consists of three stages (Figure 2.2):

(1) lung pre-segmentation: this step is based on Hu's method which is briefly summarized in subsection 2.2.1. It provides an approximate lung segmentation for the graph construction;

(2) Cost Function Computation: Based on the extracted feature information(intensity, gradient, surrounding anatomical information), kNN classifier is employed to compute voxels' unlikelihood of belonging to the lung boundary which will be used to calculate the cost function in graph;

(3) Boundary adjustment: graph search algorithm is used to adjust the boundary to obtain globally optimal segmentation surface by minimizing the cost function.

## 2.2 Geodesic Active Contour based Segmentation

### 2.2.1 Pre-segmentation - Hu's Method

Figure 2.3 shows an overview of Hu's method algorithm.

#### 2.2.1.1 Lung Extraction

Lung extraction [12] consists of three steps: optimal thresholding, connectivity and topological analysis, and airway deletion.

Optimal thresholding is applied to obtain the initial lung segmentation. Optimal thresholding algorithm selects a threshold value that is statistically optimal according to the image contents. Threshold $T_i$ is obtained iteratively according to the following formula: $T_{i+1} = \dfrac{A_0 + A_1}{2.0}$. $A_0$ is the mean gray-level of the body voxels, $A_1$ is the mean gray-level of non-body voxels (the lung and air surrounding the body)
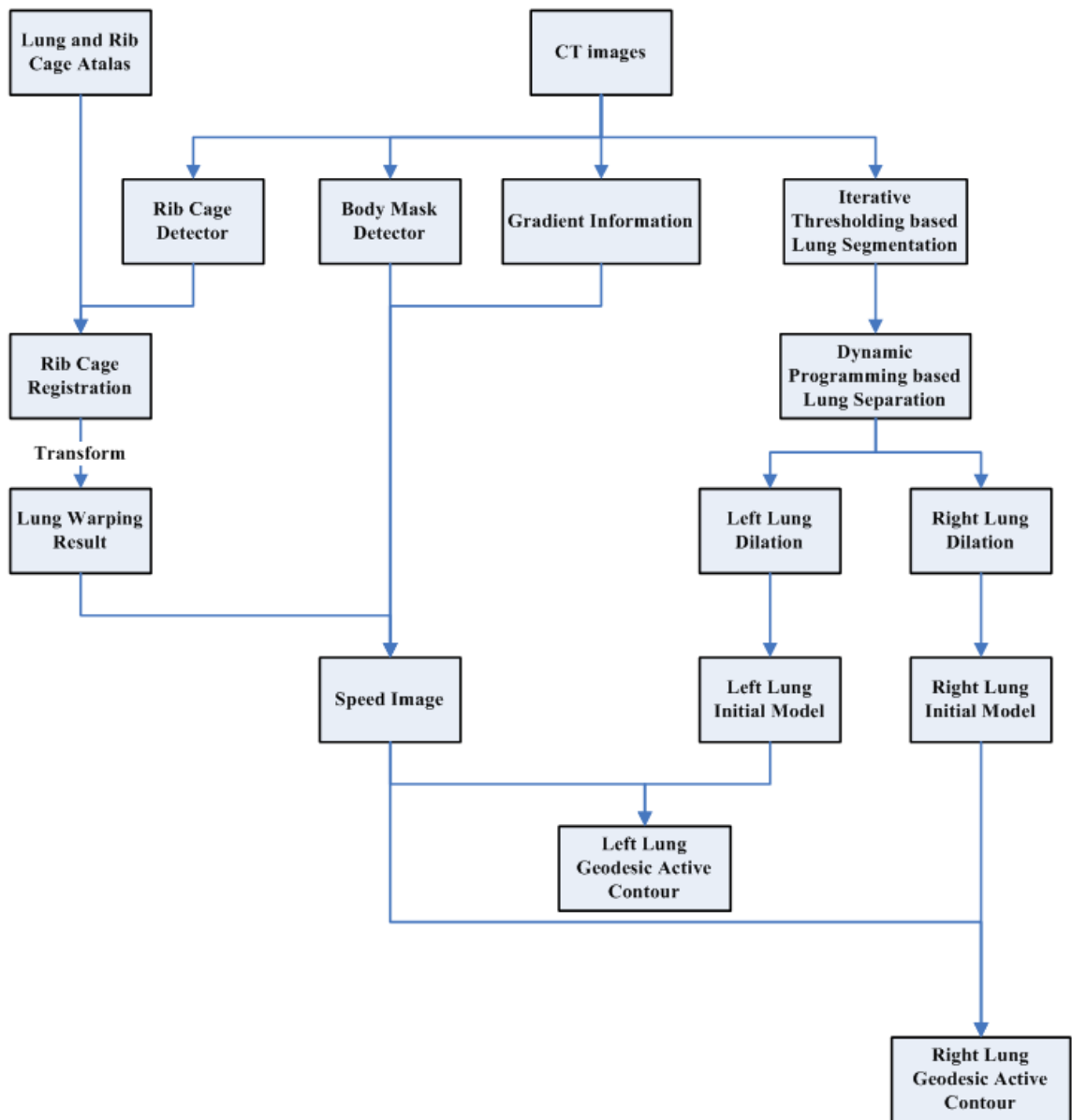
Figure 2.1: Geodesic active contour based segmentation method's algorithm flow chart.
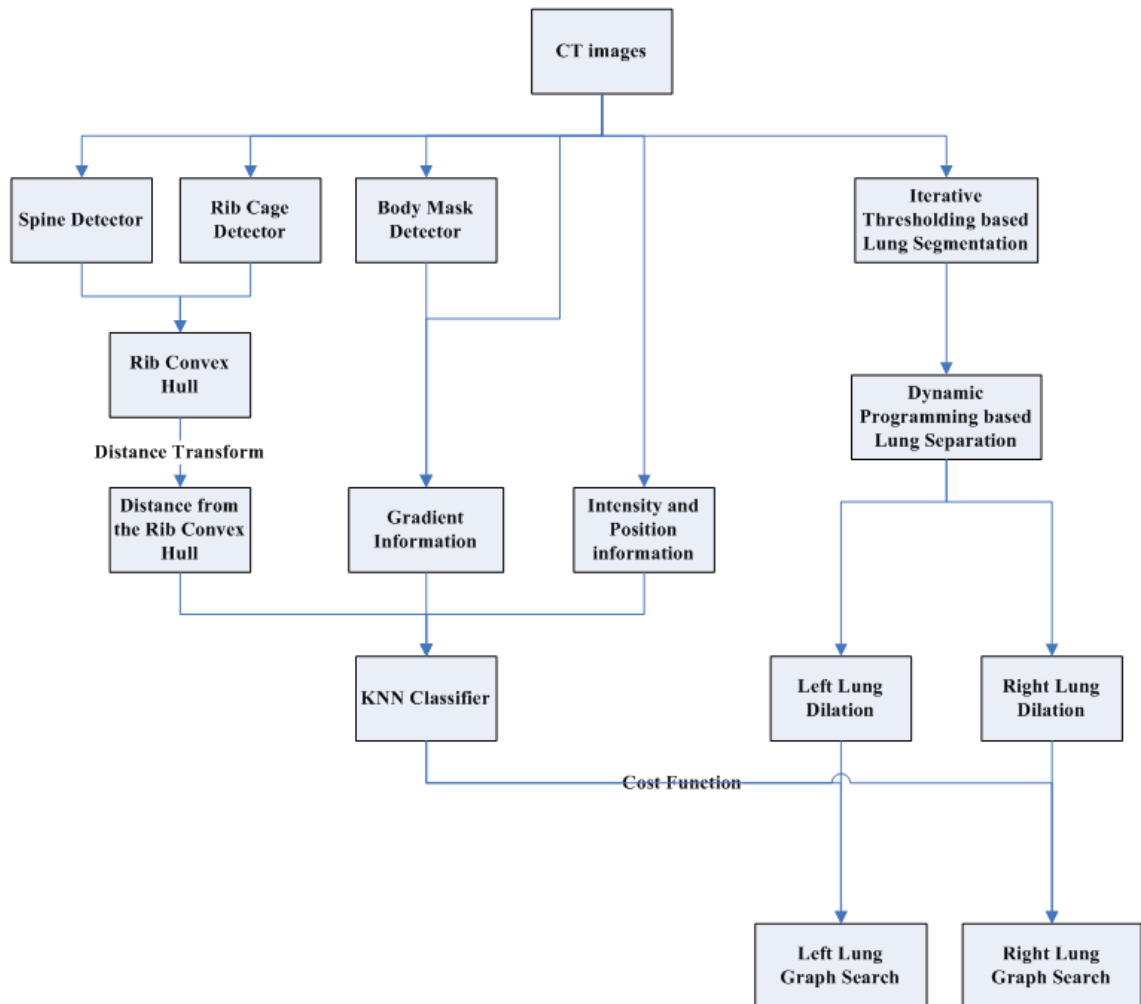
Figure 2.2: Graph search based lung segmentation method's algorithm flow chart.



Figure 2.3: Hu's method algorithm flow chart overview.

when using $T_1$ as threshold level. Iterative thresholding is repeated until there is no change in the threshold.

After obtaining the non-body voxels, 3-D connected component analysis is employed to find the lung area. Air outside the body is eliminated since these voxels are connected to the border of the image. Lung voxels are extracted since lungs are the two largest components with low gray-level and large volume greater than the pre-defined minimum volume threshold.

The trachea is identified using slice by slice region growing. The seed for region growing is detected by searching for the large, circular, air-filled region near the first few slices. The slice by slice region growing stops when the size of the region on the new slice increases dramatically, which means the airways have merged to the lung. After the extraction of the trachea and the left and right main bronchi from the image, the lung region is obtained by deleting the main airway.

### 2.2.1.2   Lung Separation

Dynamic programming is applied to separate the left lung and the right lung. Gray-level is combined into the cost function, the search region on every slice is defined by the propagation of the search region on the former slice. The 2-D erosion is used to separate the left and right lungs, and 2-D dilation is employed to find the initial search region where the separation of the left and right lungs might occur.

Post processing is applied to improve the final segmentation result. Here, a shape boundary smoothing step is added to obtain a smooth lung boundary, especially for the blood vessels near the mediastinum. Morphological closing operation is used to smooth the indentations near the mediastinum. Erosion is used to disconnect the

airway from the lung region, and then the largest connected component is applied to find the lung area, dilation is employed to restore the original approximate boundary.

### 2.2.2 Atlas-Based Registration

Due to the run time, this step is optional. If the gradient fail to provide the lung boundary information, the registration result near the spine location would be combined to the geodesic active contour speed image.

#### 2.2.2.1 Atlas Construction

The thorax CT imaging of a normal subject is chosen to be the fixed image for registration process. Thresholding followed by largest component analysis is applied to identify the rib cage since bone structures are always bright in CT images. Hu's method is employed to segment the lung region. The following figure 2.4 shows the 3D view of the fixed image used in our method which is consisted of lung region and rib cage with different labels. Figure 2.5 gives an example of the inter-subject registration process based on the rib information. In addition, figure 2.6 shows the lung region probability map (the probability of each voxel to be the lung region) by registering 10 normal thorax CT images based on the rib information.

#### 2.2.2.2 Registration of Atlas

Registration is an optimization problem of finding the correspondence between different images by minimizing the pre-defined cost function. Generally, the registration framework is consisted from 4 components: metric, transformation, interpolator, optimizer. For the metric part, there are many choices, such as mean squares, normalized correlation, mutual information. For the transformation part, we can choose
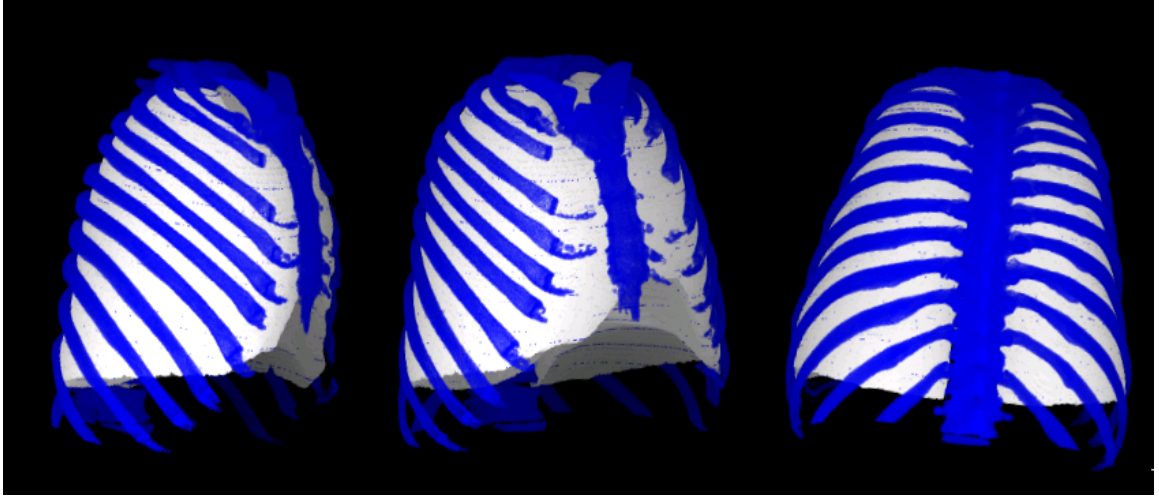
Figure 2.4: 3D view of a normal subject's Ribcage and Lung which is used as fixed image for atlas construction process in our method.

translation, rotation, scaling, affine, BSpline, other splines, etc. Optimizer is highly related to the efficiency of the converge of the registration. The most common one is the gradient descent optimizer. Regarding the interpolator, nearest neighborhood interpolator is always chosen for mask images, while the linear and BSpline interpolators are always chosen for CT images.

For this work, Elastix is used to warp the lung region probability map to the new target image by registering the rib cage. Elastix is a registration toolkit developed in 2001 by Stefan Klein, Josien P.W. Pluim, and Marius Staring. It is composed of various transformation matrices (rigid, non-rigid, affine), metrics (mutual information, mean square difference etc.), interpolators (nearest neighborhood, linear, BSplines etc.), optimization methods (gradient descent etc.).

In our work, affine followed by BSpline transformation is used to register the ribcage of the atlas to the ribcage of the new CT thorax image. Firstly, affine transformation is applied to register the ribcage of the atlas and the ribcage segmentation
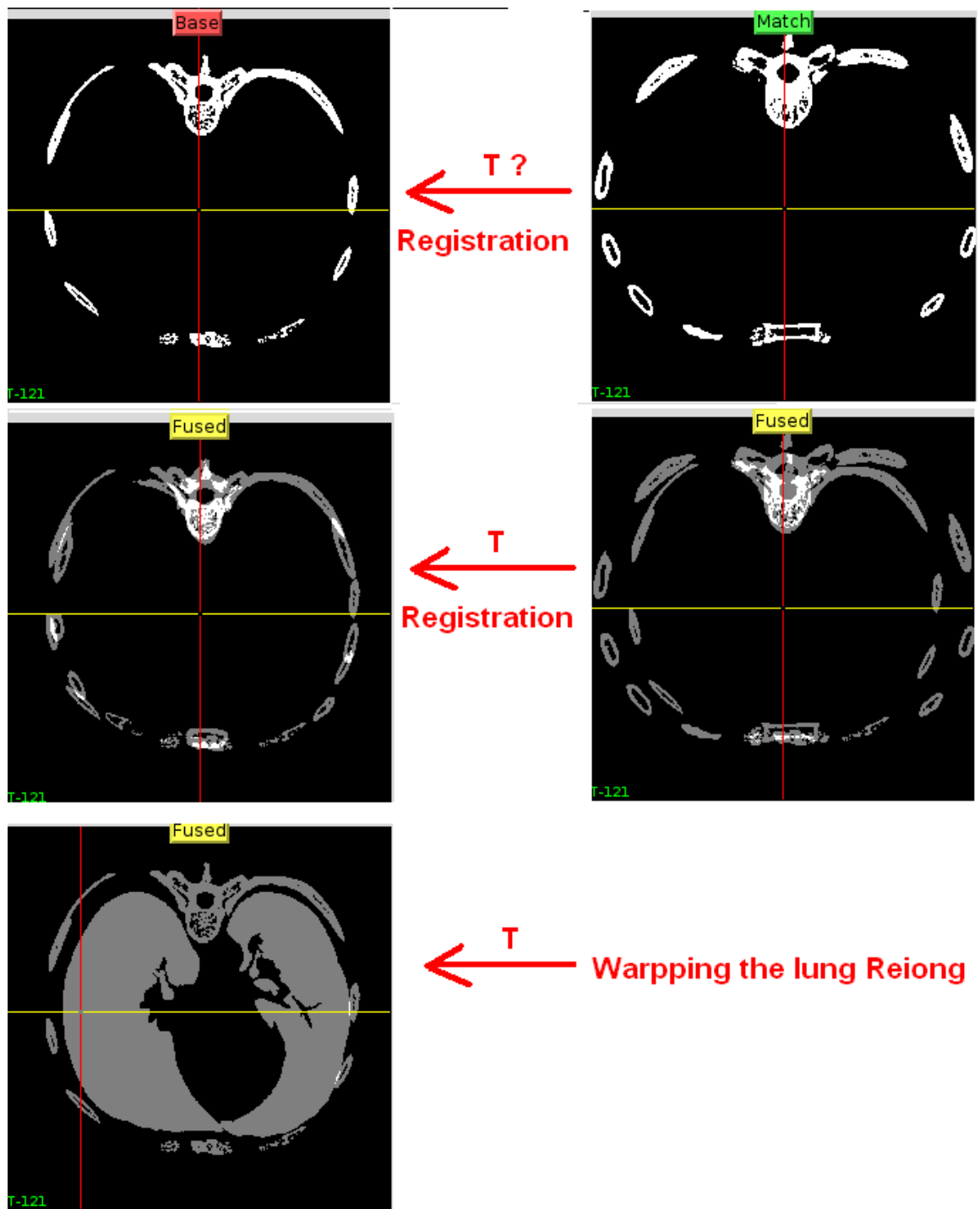
Figure 2.5: Rib information based Registration .
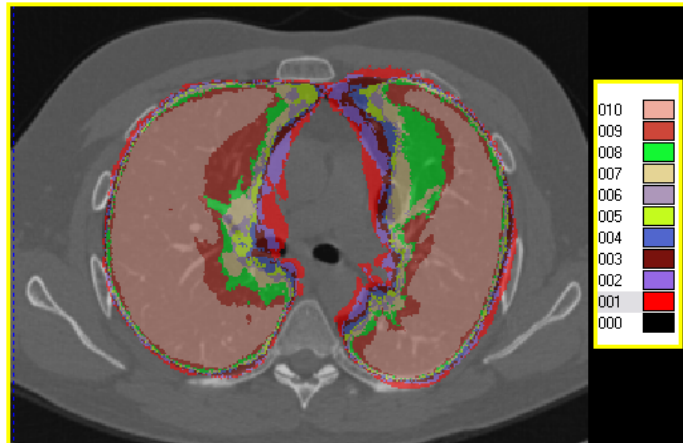
Figure 2.6: Ribcage and Lung combined Atlas used in our method.

result of the new target image. Then, BSpline transformation is used to make small regional adjustments so that the two ribcages can overlap most of the region. Transformation matrix obtained from affine and BSpline rib cage registration is used to warping the lung region probability map of the atlas to the new target CT image.

For the metric component, advanced mean squares metric is used since the registration happens between two ribcage mask images. BSpline interpolator is applied to obtain a smooth and good intensity quality of the result image. In addition, quasiNewtonLBFGS is chosen as the optimizer. Multi-resolution is employed to speed up the registration process, with image pyramid schedules 842 in each direction. Maximum iteration is 200, the maximum step length of the optimizer is $(8.0, 4.0, 2.0)$, and the minimum step length of the optimizer is $(0.5, 0.2, 0.2)$.

### 2.2.3   Boundary Adjustment

Deformable contour models could be divided into two groups [28]: the snakes and the geodesic active contour levelset. The snakes uses parametric model to represent the borders which might have intersection boundary segmentation result, while

the geodesic active contour employs the geometric deformable models to overcome this problem.

In our work Geodesic Active Contour is used to adjust the left and right lung boundaries separately. And the distance transform of Hu's method segmentation result serves as the initial segmentation for the Geodesic Active Contour, and inverse gradient information in the low intensity and high lung probability region serves as the speed image.

### 2.2.3.1  Initial Model Calculation

Initial model determines the converge of the geodesic active contour process as well as the final segmentation result. If the initial segmentation is very far away from the actual boundary, then it will take long time for the geodesic active contour converges. And the shape of the initial model will also influence the final segmentation shape. Thus, choose an initial model which is not too far away from the right answer is important.

In our work, initial left lung and right lung segmentation results obtained from the first step are dilated separately in order to make sure both the initial segmentation covers all lung possible region. After that, distance transform is applied to the dilated lung masks. The distance transform result serves as an initial model for the geodesic active contour.

### 2.2.3.2  Speed Image Calculation

The speed image plays a very important role in curve evolution process. It controls the curve evolution speed. Thus, choosing an appropriate speed image is the key of the geodesic active contour. It will also influence the efficiency of the algorithm
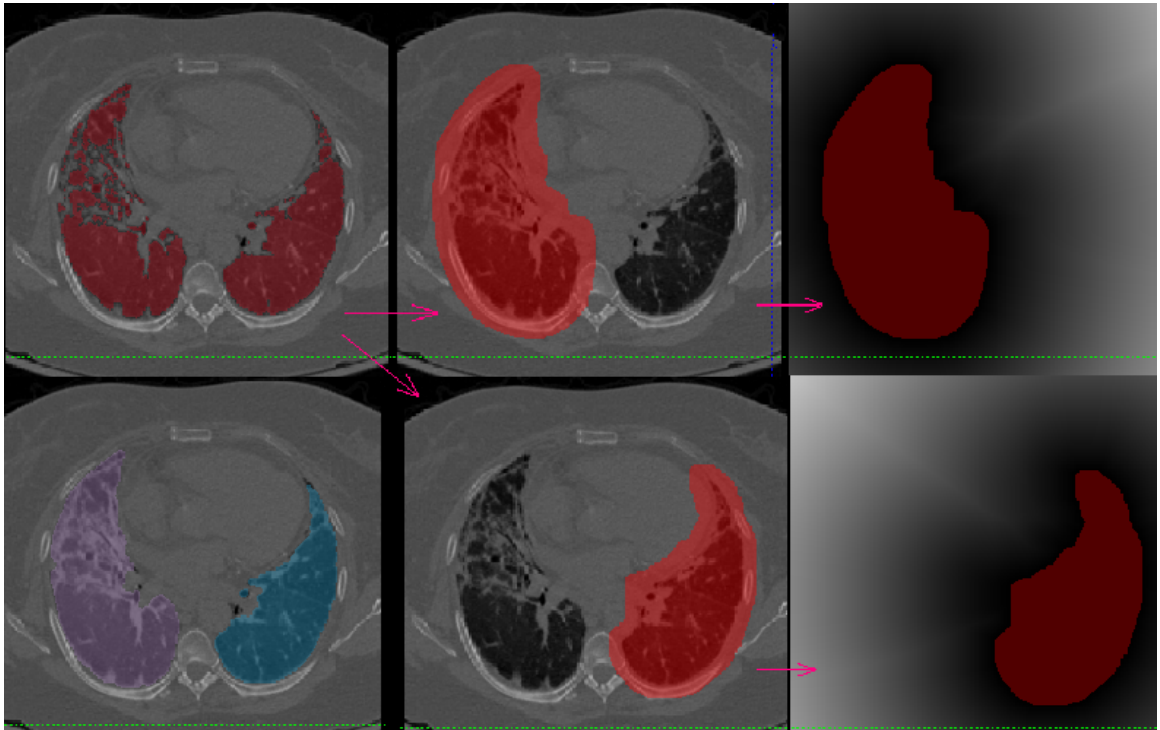
Figure 2.7: An example of initial model. From the left to the right, from the top to the bottom the figures are: the original CT image overlapped with pre-segmentation result(red), the original CT image overlapped with dilated right lung pre-segmentation result(red), the distance transform(gray-level image) overlapped with the dilated right lung, original CT image overlapped with the geodesic active contour result, the original CT image overlapped with dilated left lung pre-segmentation result(red), the distance transform(gray-level image) overlapped with the dilated left lung

and the accuracy of the final segmentation result.

In this work, main airway mask is approximately extracted by using thresholding followed by morphological opening operations. The lung region probability map detected from the atlas registration step is used to calculate the gradient. Thus, gradient calculation is only applied to the voxels inside the region where the probability is large than zero in the probability map and outside the main airway mask. After that, a low-pass filter shape function is employed to invert the gradient information. Fig 2.8 shows the transverse view of a speed image. In addition, given an CT image $I(x, y, z)$, the speed image function S(x,y,z) follows:

$$G(x, y, z) = \sqrt{\frac{\partial I^2}{\partial x} + \frac{\partial I^2}{\partial y} + \frac{\partial I^2}{\partial z}} \qquad (2.1)$$

$$S(x, y, z) = \begin{cases} \frac{1}{1+exp^{G(x,y,z)-\alpha}} & \text{for} \quad I > 0 \\ 1, otherwise \end{cases} \qquad (2.2)$$

where, $\alpha$ is set as 30.

### 2.2.3.3 Geodesic Active Contour

Geodesic active contour is an object boundaries detection approach introduced by Caselles [7] and Malladi [19]. The basic idea of the geodesic active contour is the iterative active contours evolution according to the intrinsic geometric measures of the image. The evolution direction is along the curve normal direction with the speed force given by P(C)

$$\frac{\partial C(s,t)}{\partial t} = V(C)n = (P(C)(k + w) - < \bigtriangledown P, n >)n \qquad (2.3)$$
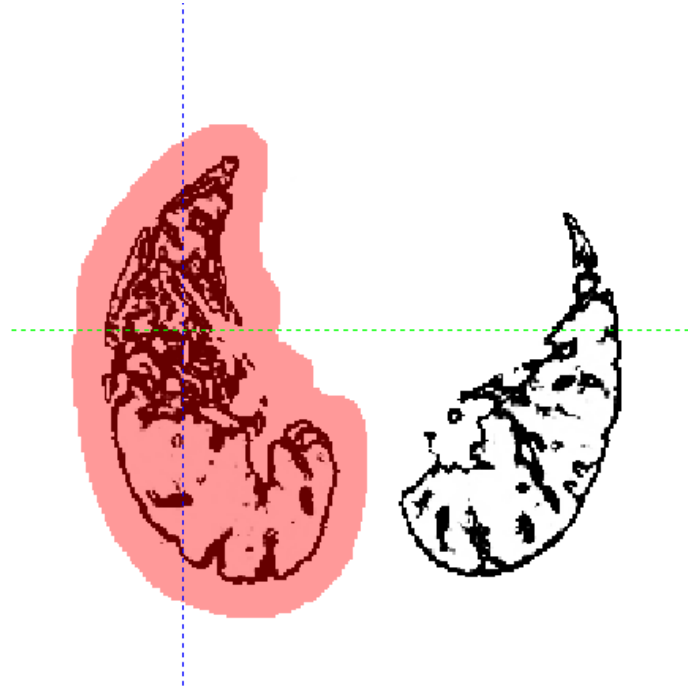
Figure 2.8: An example of speed image (dark to white corresponds to zero to one) overlapped with the initial segmentation(red).

where s is the arc length of the curve C, t is the curve evolution iteration number (for example the initial curve is C(s,0)), V(C) is the evolution speed which is dependent on the local information. The segmentation result depends on the curve evolution speed function a lot. The right equation shows a basic version of the speed function, where k is the curvature, w is the balloon force, n is the unit normal. $\bigtriangledown P$ is an attraction force projected on the normal direction. This attraction force is added in order to balance other terms and stop the curve when the curve reaches close to the boundary. In our work, the balloon force is -10 which means the initial segmentation boundaries are shrinked down to the actual lung boundaries.

Although we know the curve evolution speed of every voxel from the speed image, the curve evolution execution process remain unclear. However, the higher-dimensional function, the level set function, is used to represent the curve at different

fixed time point (or say, after different number of iterations). The following figure 2.9 gives an example of curve evolution process, the red 3-D object is the level set function, the grey images shows the curves after fixed number of iterations.
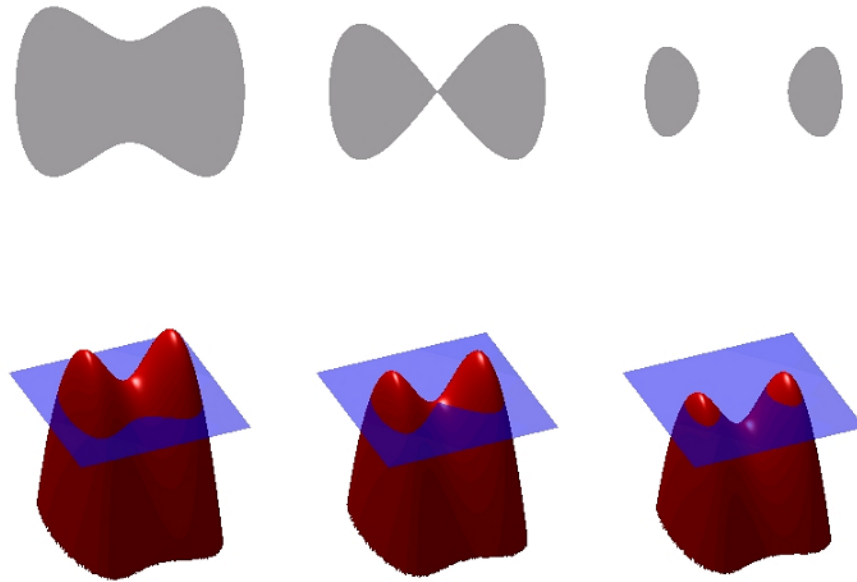


Figure 2.9: Curve evolution example. The figure is the from [3]

### 2.2.4 Post-Processing

Instead of using morphological opening, the 3-D connected component analysis is applied to both left lung and right lung geodesic active contour result images. The largest component identified in each result is the lung region. 3-D connected component is a better way to get rid of other noise points since morphological opening with large structures will cause the information loss and smoothing of the sharp corner.

After that, left lung mask and right lung mask are added together. For some cases, especially TLC cases, if the overlap of the left lung and right lung occurs, then erosion is applied to search where left lung and right lung separates, and dynamic programming is applied to obtain a nice cut between left and right lungs.

## 2.3  Graph Search based Segmentation

### 2.3.1  Rib Convex Hull Construction

Rib and spine identification is consisted of three steps: thresholding, hough transform and 3-D curve fitting. Threshold level in this work is 120 Hu since bone structures are always dense and much brighter than the lungs and muscle tissue. Hough transform followed by 3-D curve fitting is applied to detect the spinal cord region.

The spinal cord is a long tube that contains nervous tissue and support cells which are relatively darker than the vertebra in CT images. From the transverse view of thorax CT images, we can see a dark circle in the spinal cord region on almost each slice. Since the shape and size of the object is known, the spinal cord detection can be solved efficiently by Hough transform. Hough transform is a feature extraction method which tries to find the local maxima in the accumulator parameter space [28]. Since spinal cord is successfully detected on most slices, 3-D curve fitting is employed to modify the wrong detection slices by interpolation of the spinal cord locations on the previous and subsequent slices. The 3-D curve fitting is an algorithm that constructs a curve that best fits to the series of 3-D data points. The following figure shows the spinal cord detection results before and after the curve fitting process. Dilation of the spine cord detection result is used to disconnect the vertebra from the
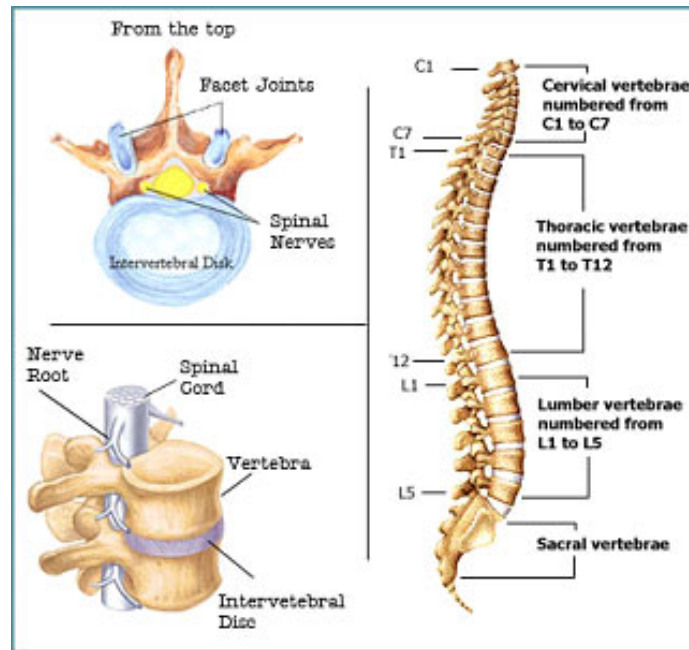
Figure 2.10: Spine Anatomy figure. The above figure is from [15]

ribs and eliminate the spine region. 3-D thinning is applied to obtain the skeleton of the ribs. Then based on the points on the rib skeleton, we construct a rib convex hull.

### 2.3.2 Cost Function Computation

K-nearest neighborhood (kNN) is a method for classifying objects based on training examples in the feature space. It is consisted of 2 steps: learning and classification. During the learning process, each voxel of the training image data is placed in the feature space with class label according to its feature value. During the classification process, each voxel of the new image data is placed in the feature space according to its feature value, and its k nearest neighbor is calculated, the probability for the voxel to belong to certain class is calculated according to equation 2.4. Each voxel is classified by a vote of its majority nearest neighbors in the feature space,
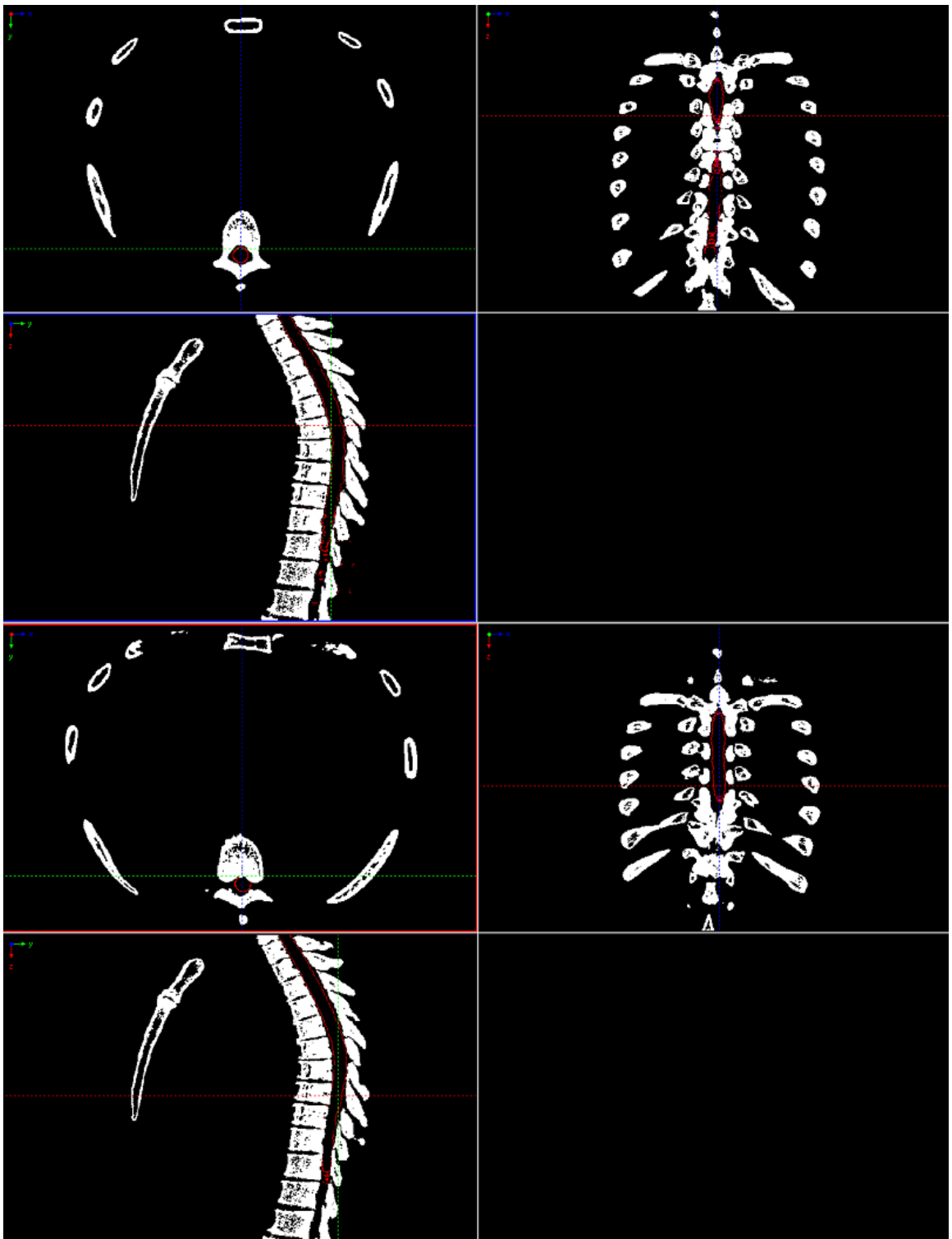
Figure 2.11: Rib detection, hough transform is used to detect the circle region of the spine(upper figure), and then 3-D curve fitting is applied to obtain a nice 3-D curve and delete the noise points (lower figure).
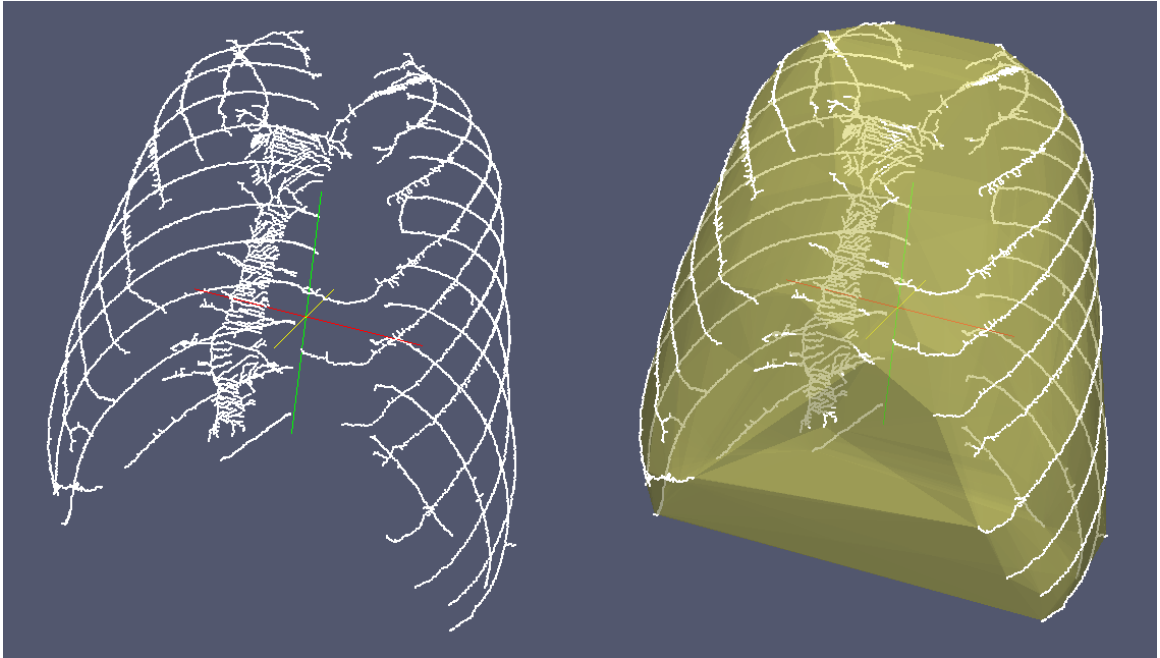
Figure 2.12: 3D thinning is applied to the ribs to obtain a skeleton, and then rib convex hull is constructed based on the rib skeleton.
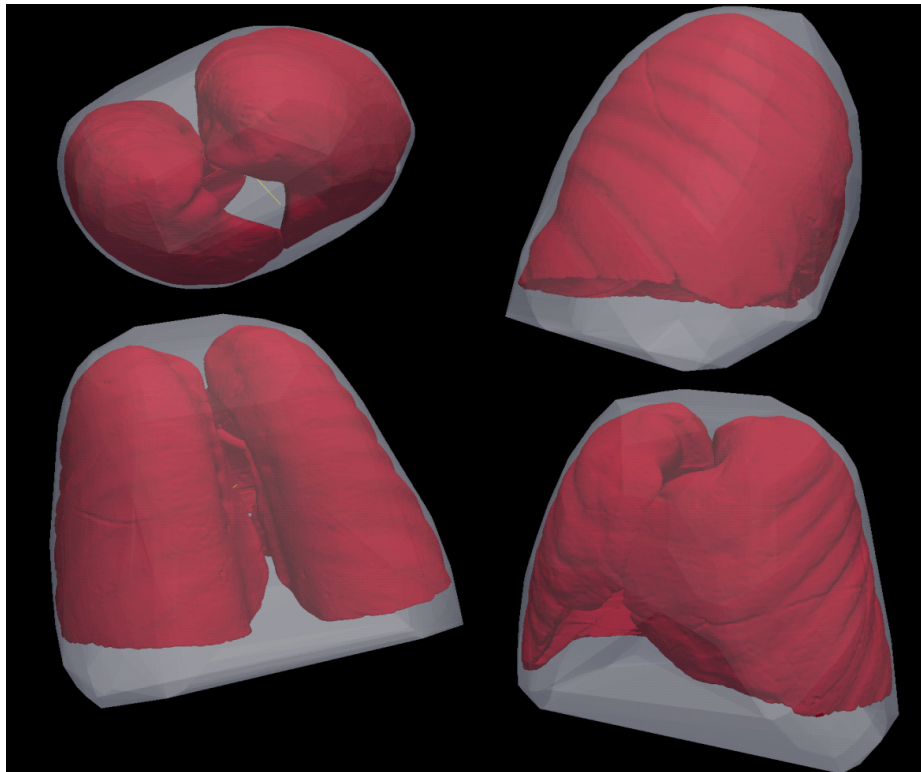


Figure 2.13: This figure shows the position relationship between rib convex hull and lung.

Figure 2.14 illustrates how kNN classifier works for classifying a new athlete as the basketball player or Ping Pong player in the 2D feature space.

$$P(x \subset classA) = \frac{n}{k} \tag{2.4}$$

, where $n$ is defined as the number of voxels from voxel $x$'s k nearest neighbor point set in the feature space that are also labeled as class A, here k equals to 10.
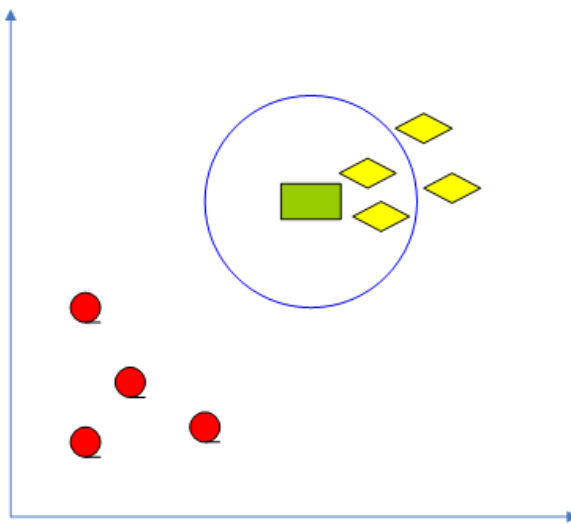


Figure 2.14: An example of knn classifier in a 2-D feature space and k=2: the horizontal axis is weight axis, the vertical axis is the height axis, the yellow diamond is the basketball player class, the red circle is the PingPong player class. The green rectangle is a new athlete that we need to judge which class he/she belongs to, the basketball or PingPong. Since the k (k=2) nearest objects of the green rectangle in the feature space is 2 yellow diamonds, thus, the probability for the green rectangle to belong to the basketball class is 1 and to the PingPong class is 0.

In our work, k is 10. In other words, each voxel is classified by a vote of its 10 nearest neighbors with distance weight in the feature space. Four pathological thorax CT image are used as training data for the kNN classifier. For each training data set, the positive pattern points are sampled from the manual lung segmentation

surface mesh, and the negative pattern points are equally sampled along normal direction of the manual lung segmentation surface mesh with distance range from -10 to 10 to the mesh. Let $I$ be the given volumetric image of $n = X \times Y \times Z$ voxels, where $X$, $Y$, $Z$ denote the image sizes in $x$, $y$, and $z$ directions, respectively. The intensity level of each voxel $(x, y, z)$ is denoted by $I(x, y, z)$. The feature vector $F = f_i(x, y, z), i = 1, 2...6$ selected to distinguish lung boundary voxels from non-lung boundary voxels is summarized in table 2.1. The detailed information about the extracted feature is listed as follows:

| Feature No | Feature Description | Image |
|---|---|---|
| 1 | intensity information | CT image |
| 2 | gradient information | CT image |
| 3 | distance from the rib convex hull | extracted rib convex hull image |
| 4 | position relative to the spine | extracted spine image |
| 5 | position relative to the spine | extracted spine image |
| 6 | position along z axis | CT image |

Table 2.1: Summary of the features selected for the kNN classifier.

(1) Gray level information: the gray level information is the value of each pixel in CT images. Each pixel value $I(x, y, z)$ of CT image represents the X-ray mass attenuation coefficient or the tissue electron density at each position. In the chest X-ray image, bones are always brighter than the lung regions because compared with the lung tissue, bones have a higher calcium, potassium, magnesium, and phosphorus percentage which will result in a higher electron density and a larger attenuation coefficient.

$$f_1(x, y, z) = I(x, y, z) \tag{2.5}$$

(2) Gradient information: Gradient is only computed for the voxels with gray level less than 0 HU and within the rib convex hull region so that large gradient cause by the rib, muscle, and other structures is eliminated. Then gradient is invert by multiplying a negative constant so that the boundary voxels with high gradient will have small value in the inverted gradient image.

$$I_x = I(x, y, z) \otimes G_x \tag{2.6}$$

$$I_y = I(x, y, z) \otimes G_y \tag{2.7}$$

$$I_z = I(x, y, z) \otimes G_z \tag{2.8}$$

$$f_2(x, y, z) = \begin{cases} 0 & I > 0 \wedge (x, y, z) \notin R \\ -\sqrt{I_x^2 + I_y^2 + I_z^2} & I < 0 \end{cases} \tag{2.9}$$

where $G$ denotes the Gaussian kernel, $R$ represents the rib convex hull region, subscript indicates the derivative, $\otimes$ is the cross convolution operation.

(3) Surrounding anatomical information: the ribs and the spine can provide an anatomical coordinate for lung segmentation. The lung outer boundary and the rib convex hull surface is very close. Thus, the distance from the rib convex hull surface can be an useful anatomical information for lung segmentation. The distance from the spine along x axis and y axis and the z value could also be useful information. Since smaller distance from the spine along x axis (in the middle part on the transverse view), larger distance from the spine along y axis (near the sternum), and larger z value(near the diaphragm) means less information could be provided by convex hull

distance (Figure 2.15). Thus, another 4 anatomical features, the distance from the rib convex hull surface, the distances from the spine along x axis and y axis, and the z value, are selected for the kNN classifier.

$$f_3(x, y, z) = min\{n \in \mathcal{N}, (x, y, z) \notin (R \ominus nB)\} \tag{2.10}$$

$$f_4(x, y, z) = x - l_x(z) \tag{2.11}$$

$$f_5(x, y, z) = y - l_y(z) \tag{2.12}$$

$$f_6(x, y, z) = z \tag{2.13}$$

where B is a 3*3 erosion structure, $\ominus$ denotes morphological erosion operation, $(l_x(z), l_y(z), z)$ is the spine cord location on the slice z.
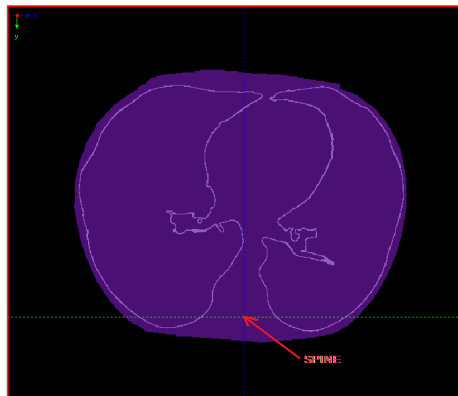


Figure 2.15: An example of the position relationship between rib convex hull surface, lung boundary and spine on transverse view.

After the feature vector extraction, each feature is normalized to have the range from 0 to 1 according to:

$$\bar{X} = \sum_{i=1}^{n} Xi \tag{2.14}$$

$$std(X) = \sum_{i=1}^{n} (Xi - \bar{X})^2 \tag{2.15}$$

$$Xi' = (Xi - \bar{X})/std(X) \tag{2.16}$$

### 2.3.3 Boundary Adjustment

Graph search is an efficient approach to obtain global optimal surface segmentation results that represent object boundaries in the volumetric data. The approach converts the segmentation problem into a min cut max flow graph problem. The time complexity of this algorithm is low-order polynomial, thus very efficient.

Graph $G(N, E)$ consists of a set of nodes $N$ and a set of edges $E$. Graph Construction starts from the presegmentation result, which contains basic topological information of the target surface. A triangulated mesh $M$ is then constructed using the marching cube method. The graph $G(N, E)$ is built based on the mesh $M$ as follows. For each vertex $v_i \in M$, a column of nodes $N(v_i, K), K = 0, 1...k...m - 1$ is created in $G$. The direction of the column is set as the triangle normal. The number of nodes in each column $m$ is determined by the required resolution. For each node $n(v_i, k)$, a node weight $w(v_i, k)$ is assigned according to the equation 2.17, in which node cost $C(v_i, k)$ is inversely related to the likelihood that the desired surface contains the node. We try to find an optimal surface $S$ such that (1) the target surface intersects with exactly one node of each column, which keeps the original topology of the presegmented surface; (2) the distance between two on-surface nodes in the neighboring columns is in the pre-defined distance, which serves as a smooth-

ness constraint; and (3) the total cost of nodes on the surface $\sum_{n(v_i,k)\in S} C(v_i,k)$ is minimized.

$$w(v_i,k) = \begin{cases} C(v_i,k) & k = 0 \\ C(v_i,k) - C(v_i,k-1) & k \in (0, m-1] \end{cases} \tag{2.17}$$

To incorporate these constraints, two types of edges are added in our graph. The intra-column edges make sure that the sought surface intersects each column exactly one time. For each node of the column $n(v_i,k)$, a directed edge $\langle n(v_i,k), n(v_i,k-1)\rangle$ with an infinite weight is added. To enforce the smoothness constraint, all nodes in the neighboring columns within pre-defined distance (the smoothness constraints $\Delta$) are connected by inter-column edges $\langle n(v_i,k), n(v_j, \max(0, k-\Delta))\rangle$. $v_i$ and $v_j$ are neighborhood vertices with neighboring relationship specified by the mesh M. Figure2.16 shows a typical example of graph construction for one 2-D slice from a 3-D image. Figure 2.17 illustrates the graph construction in our method. With the constructed graph, an optimal cut in $G$ minimizing the total node cost is computed, which corresponds to the target surface. Note that the optimal cut can be calculated efficiently using the maximum flow algorithm in a polynomial time [18].

## 2.4 Experimental Method

### 2.4.1 Validation Image Data

The lung segmentation algorithms were evaluated in two different human subjects categories: (1) thorax CT images of normal volunteers taken at different lung volumes and with B/B30 reconstruction filters; and (2) clinical thorax CT images of subjects with lung diseases, such as emphysema, fibrosis, honeycombing, nodules,
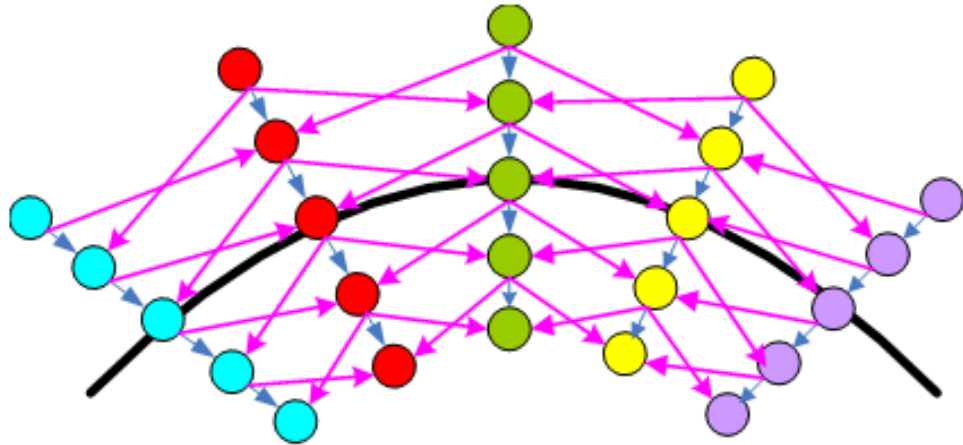
Figure 2.16: An example of graph construction for a 2D surface. Smoothness is neighborhood node distance. Blue edges are the inter-column edges, pink edges are the intra-column edges, nodes on the same column have the same color.
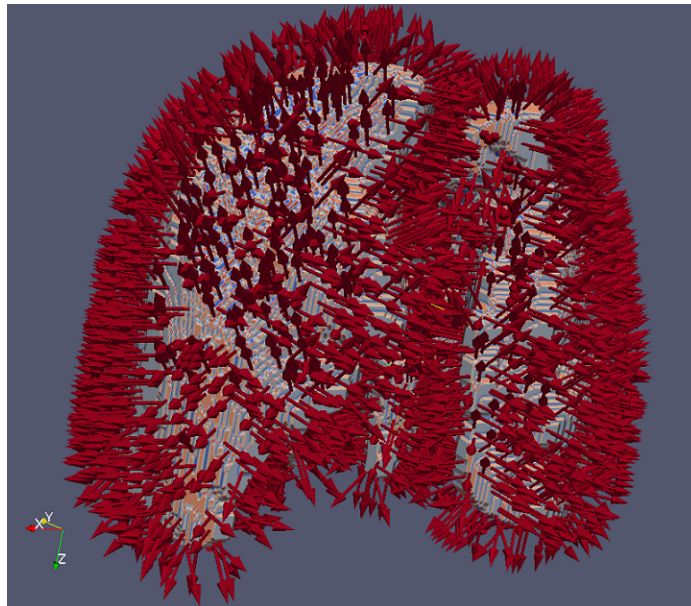


Figure 2.17: An example of graph construction for 3D surfaces. For each voxel the surface normal is computed in order to decide the direction of building the columns. The red arrow in above figure shows the surface normal direction.

bronchietasis, granulona or combined. All studies involving humans were gathered under a protocol approved by The University of Iowa institutional review board. All images were acquired on a Siemens Sensation 64 multi-detector CT scanner (MDCT) (Siemens Medical Solutions; Malverne, PA). Reconstructed slice thicknesses ranged from 0.6 to 0.9 mm. The computer used for all of the experiments was a 2.00 GHz Intel Xeon 4 core CPU workstation with 31.5 GB RAM.

Images of Normal Subjects: Data from 16 normal subjects was used to assess lung segmentation accuracy. The detailed information of these 16 subjects is shown in Table 2.2. The average age was 30.0625 years, and included 7 males and 9 females. For each subject volumetric images covering the thorax were gathered at total lung capacity (TLC) and functional residual capacity (FRC) at approximately 100 mAs. Image reconstructions were performed using a soft (B/B30) reconstruction filter from a single acquisition instead of the hard (D/B50) reconstruction filter. Considering all combinations of subjects, lung volume, and filter, 32 data sets were available in all. The automatic lung segmentation algorithm was applied to each of these data sets.

Images of Subjects with Lung Diseases: 21 clinical pathological lung CT data sets from 19 abnormal subjects (Listed in Table: 3.4) were used to assess the performance of the proposed segmentation method in the presence of lung disease. The average age was 30.855 years, and included 6 males and 13 females. Each image was read by a radiologist to confirm as abnormal lung case. 2 datasets were acquired at TLC and 19 datasets were acquired at FRC. The lung segmentation algorithm was applied to each of the 21 data sets.

The Gold Standard: To validate performance in the normal and pathological lung CT images, the automatic lung segmentation results were compared with both

| Subject ID | BRP No | Age | Gender |
|---|---|---|---|
| 1 | $brp001$ | 38 | $Male$ |
| 2 | $brp016$ | 23 | $Female$ |
| 3 | $brp148$ | 28 | $Male$ |
| 4 | $brp028$ | 37 | $Female$ |
| 5 | $brp031$ | 24 | $Male$ |
| 6 | $brp042$ | 24 | $Female$ |
| 7 | $brp043$ | 44 | $Female$ |
| 8 | $brp047$ | 23 | $Male$ |
| 9 | $brp067$ | 20 | $Male$ |
| 10 | $brp072$ | 22 | $Female$ |
| 11 | $brp076$ | 20 | $Female$ |
| 12 | $brp133$ | 24 | $Female$ |
| 13 | $brp136$ | 26 | $Female$ |
| 14 | $brp038$ | 60 | $Female$ |
| 15 | $brp037$ | 27 | $Male$ |
| 16 | $brp035$ | 41 | $Male$ |

Table 2.2: Information of Normal Subjects.

| Subject ID | BRP No | Age | Gender | Detail information |
|---|---|---|---|---|
| 1 | $BPD916$ | 1.25 | $Female$ | $prematurebaby$ |
| 2 | $0639Z$ | 26 | $Female$ | $asthma$ |
| 3 | $1279A$ | 27 | $Female$ | $asthma$ |
| 4 | $brp019$ | 27 | $Male$ | $benignnodule$ |
| 5 | $brp021$ | 33 | $Female$ | $benignnodule$ |
| 6 | $0904S$ | 25 | $Female$ | $asthma$ |
| 7 | $1257Q$ | 52 | $Female$ | $asthma$ |
| 8 | $brp025$ | 38 | $Male$ | $COPD, nodule$ |
| 9 | $0840S$ | 38 | $Female$ | $asthma$ |
| 10 | $1275S$ | 20 | $Female$ | $asthma$ |
| 11 | $1623P$ | 46 | $Female$ | $asthma$ |
| 12 | $1818E$ | 27 | $Male$ | $asthma$ |
| 13 | $brp075$ | 22 | $Female$ | $nodule$ |
| 14 | $brp022$ | 36 | $Male$ | $nodule$ |
| 15 | $brp005$ | 35 | $Male$ | $nodule$ |
| 16 | $brp084$ | 40 | $Female$ | $nodule, airtrapping$ |
| 17 | $brp008$ | 25 | $Male$ | $honeycombingtexture, bronchiectasis$ |
| 18 | $1194S$ | 21 | $Female$ | $asthma$ |
| 19 | $1771E$ | 47 | $Female$ | $asthma$ |

Table 2.3: Information of Abnormal Subjects.

a manually defined gold-standard and Hu's method results. A human image analyst manually traced the lung boundaries for each of the 53 data sets. Due to the large size of the MDCT images (typically 512*512*500), manual segmentation is done by editing Hu's method segmentation result slice by slice from the transverse view.

### 2.4.2  Validation Criteria

Three criteria were used to compare the proposed method with Hu's and Method manual tracing. Sensitivity and specificity were used to measure the volume overlap, while the hausdorff distance was employed to measure the border position accuracy. In addition, the treat off between the run time and the segmentation accuracy is analyzed in chapter 3. Geodesic active contour based method was tested on these 53 data sets(21 abnormal CT images and 32 normal CT images), while graph search based method was trained by 4 abnormal CT images and tested on 6 pathological CT data sets.

Paired-sample t-test was applied to evaluate whether our methods has significant improvement compared with Hu's method. Paired-sample t-test is a statistical hypothesis test. It is used to compare two sets of measurements in order to assess whether their population means differ. Since sensitivity, specificity, and Hausdorff distance were computed for both Hu's method and our methods on the same test data set, paired-sample t-test was used to compare the performance of our method and Hu's method. For example, it was used to see if our methods' sensitivity is significantly higher than Hu's method's sensitivity. In addition, paired-sample t-test was applied to evaluate whether our methods' Hausdorff distance is significantly smaller than Hu's method's Hausdorff distance.

(1) sensitivity and specificity

sensitivity and specificity could be used as statistical measures of the segmentation algorithm performance. Given the manual segmentation as the gold standard, we computed sensitivity and specificity for both our methods results and Hu's method results.

Sensitivity, true positive rate, is the portion of the actual lung tissue pixel in the manual segmentation mask that are detected by the segmentation algorithm. Thus, sensitivity evaluates how effective of the segmentation algorithm when used on lung pixels. The algorithm is perfect for lung pixel detection if the sensitivity is 1, and random if the sensitivity is 0.5. The mathematical formula for calculating sensitivity is given by:

$$Sensitivity = \frac{TruePositive}{TruePositive + TrueNegative} \qquad (2.18)$$

, where true positive means the pixel is both inside the manual segmentation lung mask and the automatic segmentation lung mask, and true negative means the pixel is inside the manual segmentation lung mask but outside the automatic segmentation lung mask.

Specificity, true negative rate, is the portion of the actual background pixel in the manual segmentation mask that are detected as background by the segmentation algorithm. Thus, specificity illustrates how effective of the segmentation algorithm when used on background pixels. The algorithm is perfect for background pixel detection if the specificity is 1, and random if the specificity is 0.5. The mathematical

formula for calculating specificity is given by:

$$specificity = \frac{FalsePositive}{FalsePositive + FalseNegative} \qquad (2.19)$$

, where false positive means the pixel is both outside the manual segmentation lung mask and the automatic segmentation lung mask, and false negative means the pixel is outside the manual segmentation lung mask but inside the automatic segmentation lung mask.

(2) Border position accuracy:

Since the lungs have large volumes, high volume overlap rate could not measure the small local boundary error. Hence, the Hausdorff distance between the manually-defined lung boundaries and the computer-defined lung boundaries was used to access the border position accuracy. Hausdorff distance measures the largest surface distance between two contours by computing the distance between the set of non-zero voxels of two image contours using the following formula.

$$where h(A, B) = max_{a \in A} min_{b \in B} ||a - b||, . \qquad (2.20)$$

$$H(A, B) = max(h(A, B), h(B, A)); \qquad (2.21)$$

(3) Effects of interpolated image resolution on runtime and segmentation accuracy

The boundary adjustment step (the geodesic active contour process) accounts for a large part of runtime which heavily depends on the image size. Thus, we performed an experiment to examine the tradeoffs between runtime and accuracy

during the boundary adjustment step. For each of the five abnormal thorax CT images, we segmented the lung boundary at three different scales.

# CHAPTER 3
# RESULTS

## 3.1    Evaluate Geodesic Active Contour based Method

The geodesic active contour based method was evaluated by 21 clinical thorax
CT images of 19 subjects with lung diseases, such as emphysema, fibrosis, honey-
combing, nodules or combined, and 32 thorax CT images of 16 normal subjects.
Sensitivity, specificity, Hausdorff distance, number of slices needed to edit, and time
efficiency were used as criteria to compare the geodesic active contour based method
with the Hu's method.

In order to visually compare Hu's method and our method, figure  3.1 gives
two examples of the pathological lung segmentation results of the geodesic active
contour based method, Hu's method and manual tracing.

### 3.1.1   Segmentation Sensitivity

Sensitivity evaluates how effective of the segmentation algorithm when used
on lung pixels. The algorithm is perfect for lung pixel detection if the sensitivity
is 1, and random if the sensitivity is 0.5. The larger the sensitivity is, the better
the segmentation result is. Figure 3.2 illustrates the sensitivity of 21 abnormal lung
CT data sets using both the geodesic active contour based method results and Hu's
method results with manual segmentation ground truth. Figure 3.3 illustrates the
sensitivity of 32 normal lung CT data sets using both the geodesic active contour
based method results and Hu's method results with manual segmentation ground
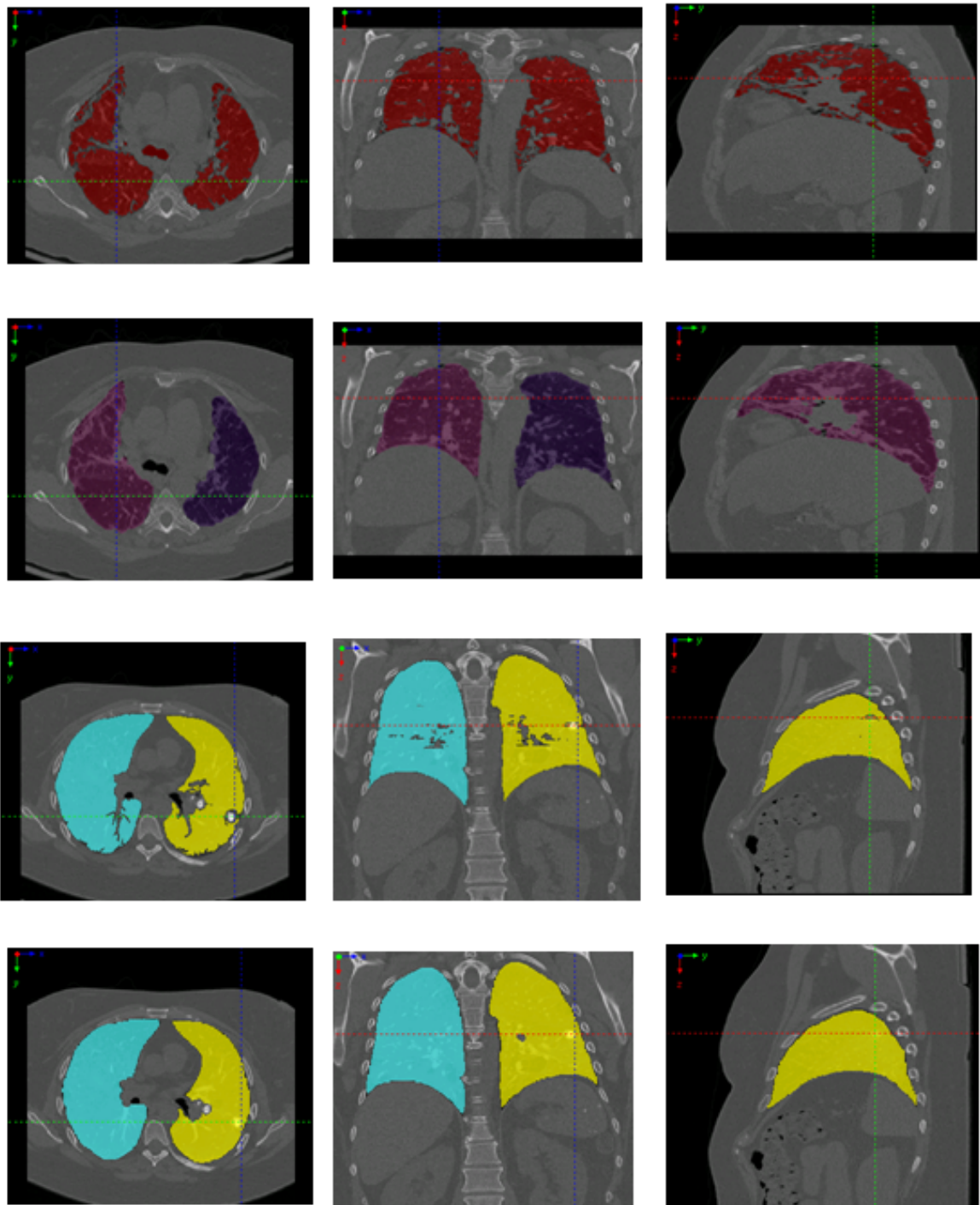truth. The dark blue bars represent the sensitivity of the geodesic active contour

Figure 3.1: Geodesic active contour result of 2 cases. From left to right: transverse view, cornal view, and sagittal view. First row: Hu's method segmentation result of case 1, second row: our method segmentation result of case 1, third row: Hu's method segmentation result of case 2, fourth row: our method segmentation result of case 2.

based method, the light blue bars represent the sensitivity of Hu's method. In the figures, the dark blue bars are the sensitivity of the geodesic active contour based method segmentation result, while the light blue bars are the sensitivity of the Hu's method segmentation result. In figure 3.2 the light blue bars are always shorter than the dark blue bars which means that for pathological lung data set the geodesic active contour based method has a higher sensitivity than Hu's method. In figure 3.3 the light blue bars are almost the same as the dark blue bars which means that for normal lung data set the geodesic active contour based method has similar sensitivity as Hu's method. One side paired t-test was employed to measure whether two methods are statistically significant different with respect to the sensitivity. For 21 abnormal CT images, the sensitivity of the geodesic active contour based method was 5.9% larger on average than that of Hu's method (statistically significant, $p < 0.001$). For 32 normal CT images, the sensitivity of the geodesic active contour based method was 0.7% larger on average than that of Hu's method (statistically insignificant, $p = 0.11$). Thus, from the sensitivity aspect, we could conclude for pathological lung CT data set the geodesic active contour based method has better performance than Hu's method, and for normal lung CT data set these two methods are almost the same.

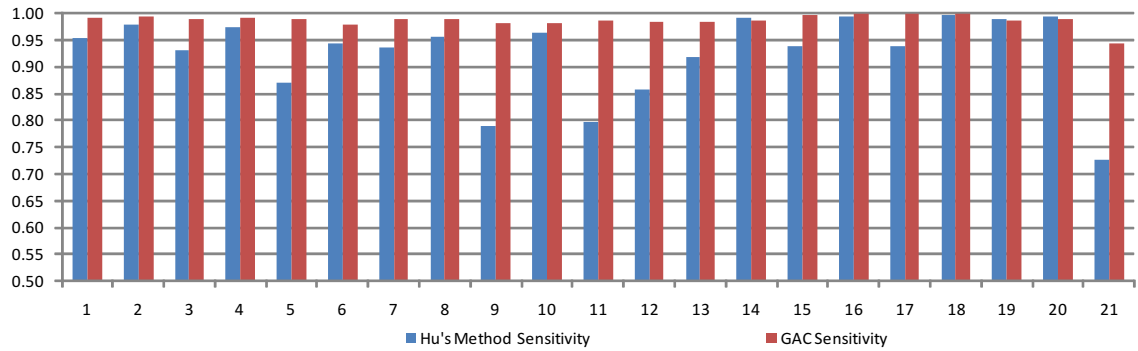| Dataset Category | Hu's Method | GAC Method |
|---|---|---|
| *Normal* | $0.985 \pm 0.027$ | $0.992 \pm 0.006$ |
| *Abnormal* | $0.928 \pm 0.073$ | $0.987 \pm 0.011$ |

Table 3.1: Sensitivity statistics summary.

Figure 3.2: Sensitivity analysis plot of geodesic active contour based method on 21 abnormal thorax CT data sets.
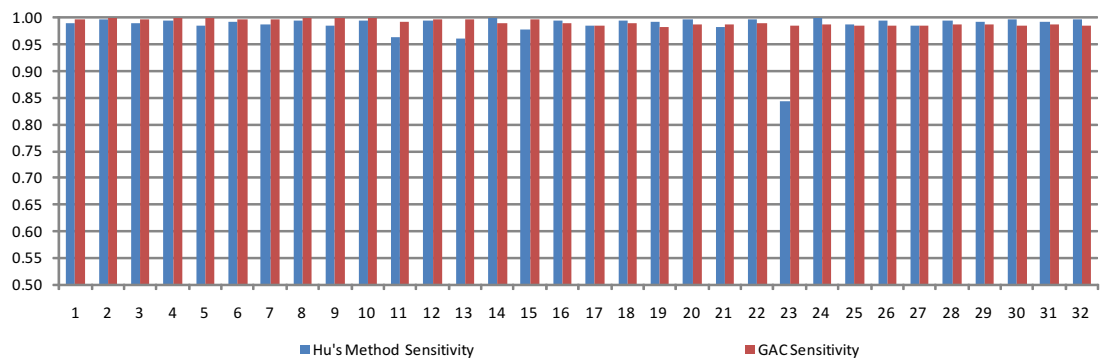


Figure 3.3: Sensitivity analysis plot of geodesic active contour based method on 32 normal thorax CT data sets.

### 3.1.2 Segmentation Specificity

Specificity illustrates how effective of the segmentation algorithm when used on background pixels. The algorithm is perfect for background pixel detection if the specificity is 1, and random if the specificity is 0.5. The larger the specificity is, the better the segmentation result is. Figure 3.4 illustrates the sensitivity of 21 CT data sets using both the geodesic active contour based method results and Hu's method results with manual segmentation ground truth. The dark blue bars represent the specificity of the geodesic active contour based method, the light blue bars represent the specificity of Hu's method. In the figures, the dark blue bars are the specificity of the geodesic active contour based method segmentation result, while the light blue bars are the specificity of the Hu's method segmentation result. In the figure 3.4, 3.5, The dark blue bars are almost the same as the light blue bars which means that the geodesic active contour based method has similar specificity as Hu's method. One side paired t-test was employed to measure whether two methods are statistically significant different with respect to the specificity. For 21 abnormal CT images, the specificity of the geodesic active contour based method was 0.3% smaller on average than that of Hu's method (statistically significant, $p < 0.001$). For 32 normal CT images, the sensitivity of the geodesic active contour based method was 0.3% smaller on average than that of Hu's method (statistically significant, $p < 0.001$). Although the specificity of Hu's method is statistically significant higher than that of geodesic active contour based method, the specificity of both two methods is above 0.99 which is near 1. Thus, we could conclude that for both abnormal and normal lung CT data sets, Hu's method is more conservative than geodesic active contour based method.
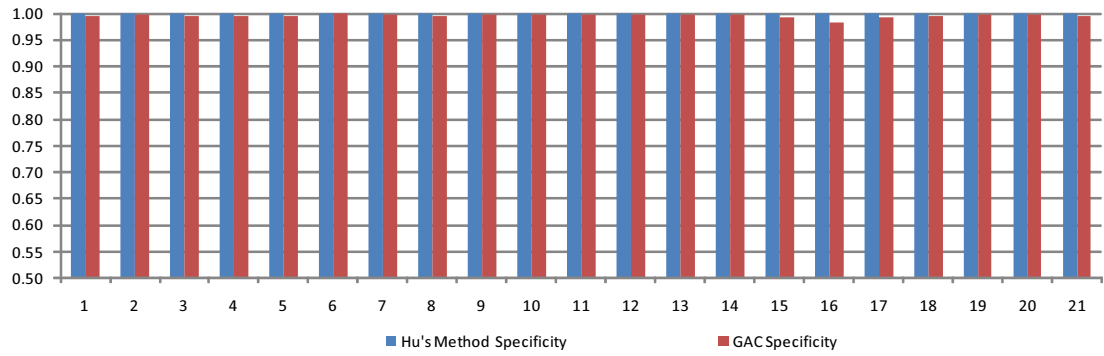
Figure 3.4: Specificity analysis plot of geodesic active contour based method on 21 abnormal thorax CT data sets.
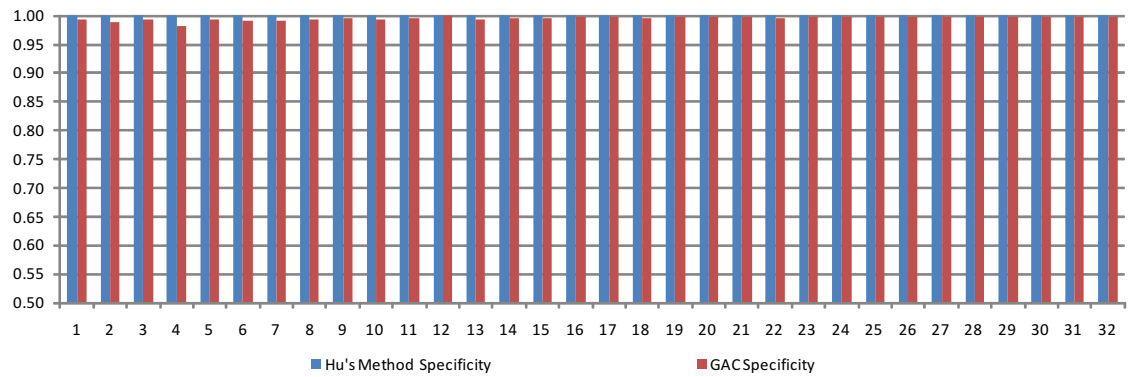


Figure 3.5: Specificity analysis plot of geodesic active contour based method on 32 normal thorax CT data sets.

| Dataset Category | Hu's Method | GAC Method |
|---|---|---|
| *Normal* | $0.999 \pm 0.0001$ | $0.996 \pm 0.003$ |
| *Abnormal* | $0.999 \pm 0.0002$ | $0.996 \pm 0.003$ |

Table 3.2: Specificity statistics summary.

### 3.1.3    Boundary Position Accuracy

Since the lungs have large volumes, high volume overlap rate could not measure the small local boundary error. Hence, the Hausdorff distance between the manually-defined lung boundaries and the computer-defined lung boundaries was used to access the border position accuracy. Hausdorff distance measures the largest surface distance between two contours by computing the distance between the set of non-zero voxels of two image contours. The algorithm is perfect for background pixel detection if the Hausdorff distance is 0. The smaller the Hausdorff distance is, the better the segmentation result is. Figure 3.6 illustrates the Hausdorff distance of 21 abnormal CT data sets using both the geodesic active contour based method results and Hu's method results with manual segmentation ground truth. Figure 3.7 illustrates the Hausdorff distance of 32 normal CT data sets using both the geodesic active contour based method results and Hu's method results with manual segmentation ground truth. The dark blue bars represent the Hausdorff distance of the geodesic active contour based method, the light blue bars represent the Hausdorff distance of Hu's method. In figure 3.6, 3.7, the dark blue bars are the Hausdorff distance of the geodesic active contour based method segmentation result, while the light blue bars are the Hausdorff distance of the Hu's method segmentation result. For most abnormal and normal cases, the dark blue bars are shorter than the light blue bars which means that the geodesic active contour based method has shorter Hausdorff distance than Hu's method. One side paired t-test was employed to measure whether two methods are statistically significant different with respect to the Hausdorff distance. For 21 abnormal CT images, the Hausdorff distance of the geodesic active contour based method was 12.65 pixel smaller on average than that of Hu's method

(statistically significant, $p < 0.001$). For 32 normal CT images, the sensitivity of the geodesic active contour based method was 6.97 pixel smaller on average than that of Hu's method (statistically significant, $p < 0.002$). Thus, from the Hausdorff distance aspect we could conclude that geodesic active contour based method is better than Hu's method for both normal and abnormal thorax CT data sets.
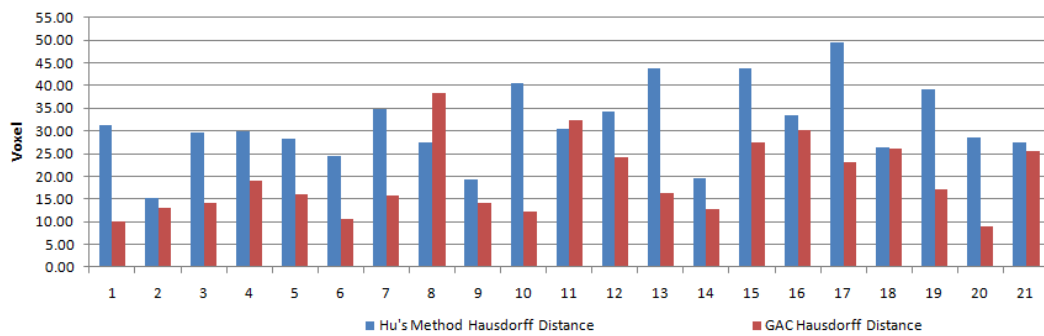


Figure 3.6: Hausdorff Distance analysis plot of geodesic active contour based method on 21 abnormal thorax CT data sets.
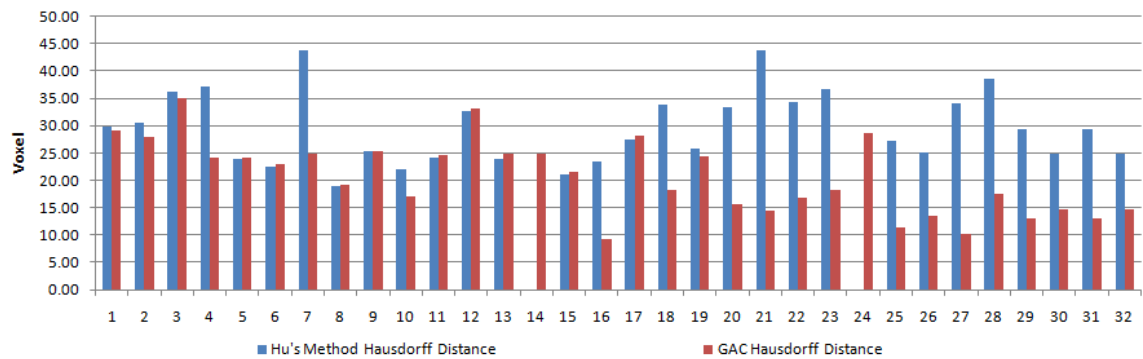


Figure 3.7: Hausdorff Distance analysis plot of geodesic active contour based method on 32 normal thorax CT data sets.

| Dataset Category | Hu's Method(unit: pixel) | GAC Method(unit: pixel) |
|---|---|---|
| *Normal* | $27.60 \pm 9.63$ | $20.63 \pm 6.70$ |
| *Abnormal* | $32.80 \pm 9.65$ | $20.15 \pm 8.15$ |

Table 3.3: Hausdorff distance statistics summary.

### 3.1.4 Trade Off between Run time and Accuracy

The geodesic active contour process accounts for a large part of runtime which heavily depends on the image size. Thus, we performed an experiment to examine the tradeoffs between runtime and accuracy during the boundary adjustment step. For each of the 5 abnormal thorax CT images, we segmented the lung boundary at three different scales. Figure 3.8, 3.9, 3.10 illustrate the running time at three different scales. For scale 0, the image size was $512 * 512 * slicenumber$; for scale 1, the image size was $256 * 256 * slicenumber/2$; for scale 2, the image size was $128 * 128 * slicenumber/4$. Figure 3.11 illustrates the relationship between the mean and standard deviation of the running time and the image size.
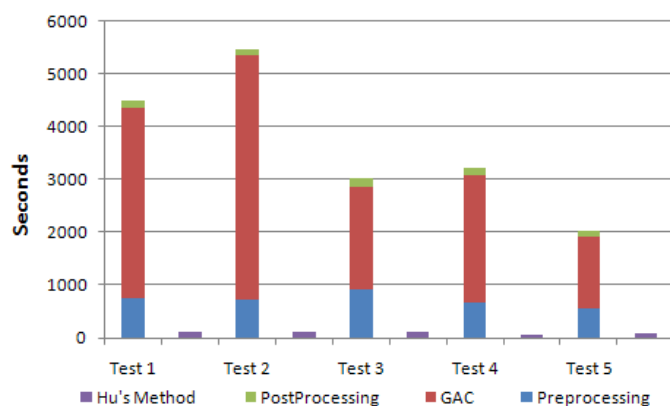


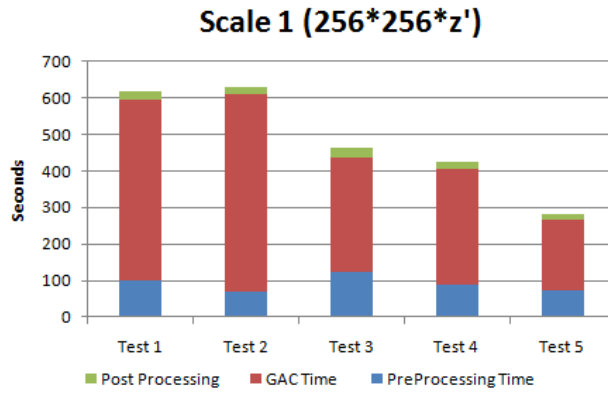Figure 3.8: Running time plot of 5 test CT data set at scale 0.

Figure 3.9: Running time plot of 5 test CT data set at scale 1 .
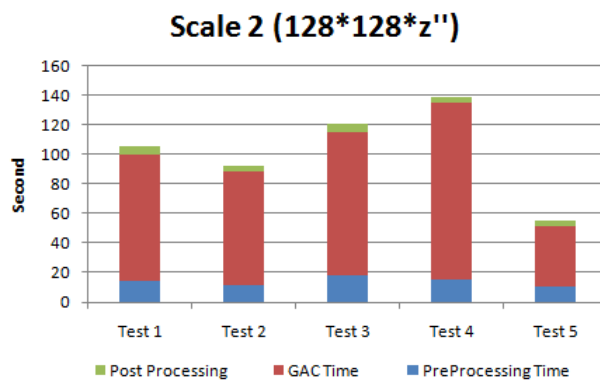


Figure 3.10: Running time plot of 5 test CT data set at scale 2.
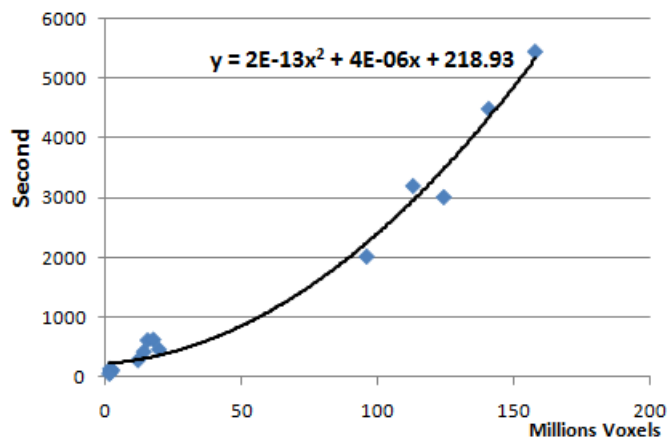


Figure 3.11: This figure illustrates the relationship between the running time and the image size.

| Scale | Time(s) | Sensitivity | Specificity | Hausdorff Distance(unit:pixel) |
|-------|---------|-------------|-------------|-------------------------------|
| 0 | $3634.8 \pm 600.5718$ | $0.970 \pm 0.040$ | $0.997 \pm 0.003$ | $19.52 \pm 6.41$ |
| 1 | $483 \pm 64.3374$ | $0.939 \pm 0.053$ | $0.998 \pm 0.001$ | $22.13 \pm 6.49$ |
| 2 | $102.4 \pm 14.2253$ | $0.877 \pm 0.061$ | $0.998 \pm 0.001$ | $42.71 \pm 14.93$ |

Table 3.4: Mean and standard deviation of the running time of the 5 test CT data set at three different scales.



Figure 3.12: This figure shows the geodesic active contour based method results on three different scales. From left to right: scale0, scale1, scale0, where $Z$ denotes the total slice number of the CT image data sets.



Figure 3.13: This figure shows the enlarged geodesic active contour based method results on three different scales. From left to right: scale2, scale1, scale0.

### 3.1.5 Multi-threading

With the advancement in the computer hardware, multi-threading is becoming an increasingly important since it can speed up the program by making best use of available CPU cycles. On a si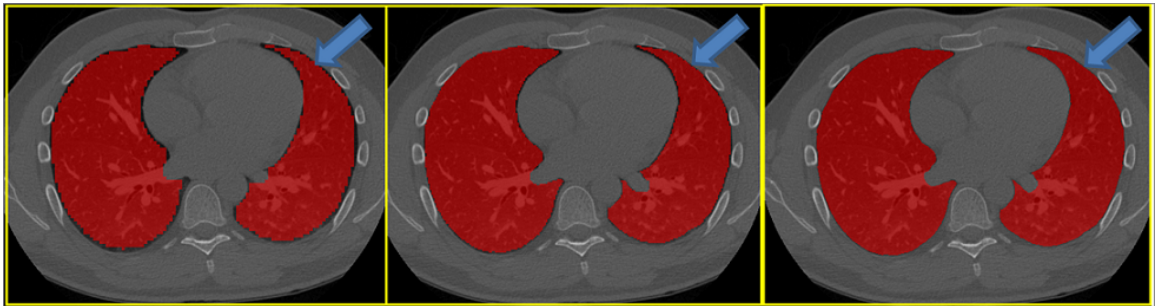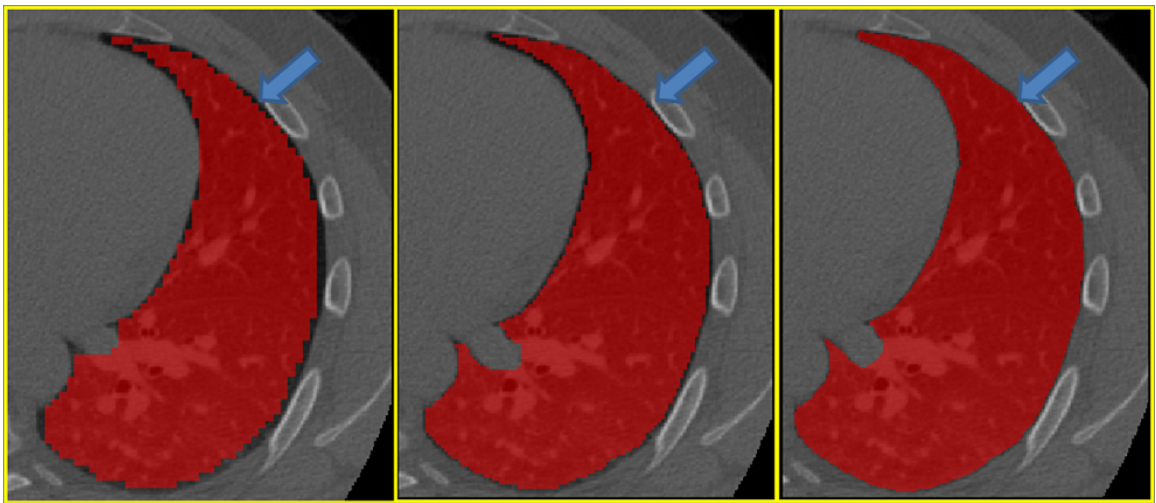ngle-core computer, multi-threading is done by switching the processor between different threads. While on a multi-core computer, multi-threading is accomplished by running multiple threads at the same time, with each CPU running a particular thread. Since all the experiments were done on a 2.00 GHz Intel Xeon 4 core CPU workstation with 32 GB RAM, we could run multi-task at the same time on different cores. For example, initial model and speed image were computed concurrently, the left lung boundary adjustment and right lung boundary adjustment happened at the same time one different cores. A summary of the run time improvement by multi-threading is shown in table 3.5 and figure 3.14. We could find that the run time of the multi-threading program is half of the single thread geodesic active contour based program. It takes around 5 minutes to run the geodesic active contour based method on one CT data set at scale 1.

| Method | Preprocessing | GAC | Postprocessing | Total |
|---|---|---|---|---|
| *Singlethreading* | $91.8 \pm 21.6$ | $371.4 \pm 143.4$ | $19.8 \pm 3.34$ | $483.0 \pm 143.8$ |
| *Multithreading* | $54.8 \pm 7.49$ | $200.0 \pm 90.0$ | $16.8 \pm 4.32$ | $271.6 \pm 94.79$ |

Table 3.5: Run time of the geodesic active contour based method implementations with and without multi-threading on five test CT image at scale 1.(unit: second).
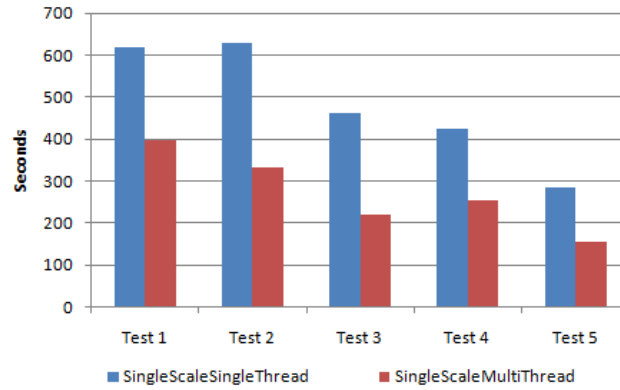
Figure 3.14: Runtime comparison plot between single thread implementation and multi-thread implementation on five test data sets.

## 3.2  Evaluate Graph Search Based Method

The graph search based method was evaluated by 15 clinical thorax CT images of 15 subjects with lung diseases, such as emphysema, fibrosis, honeycombing, nodules or combined. To validate performance in the pathological lung CT images, the graph search based pathological lung segmentation results were compared with both a manually defined gold-standard and Hus method results. Three criteria, sensitivity, specificity, and Hausdorff distance, were used to compare the graph search based method with Hu's method and manual segmentation.

In order to visually compare Hu's method and graph search based method, figure 3.15 gives one examples of the pathological lung segmentation results of the graph search based method, Hu's method and manual tracing.

### 3.2.1  Segmentation Sensitivity

Sensitivity evaluates how effective of the segmentation algorithm when used on lung pixels. The algorithm is perfect for lung pixel detection if the sensitivity is 1, and random if the sensitivity is 0.5. The larger the sensitivity is, the better the

Figure 3.15: Examples of lung segmentation result, from left to right: Hus method result, manual segmentation, graph-search based method result.

segmentation result is. Figure 3.16 illustrates the sensitivity of 15 abnormal lung CT data sets using both the graph search based method results and Hu's method results with manual segmentation ground truth. In figure 3.16, the red bars represent the sensitivity of the graph search based method, while the blue bars represent the sensitivity of Hu's method. The blue bars are always shorter than the red bars which means that for pathological lung data set the graph search based method has a higher sensitivity than Hu's method. The table 3.6 shows the sensitivity of the graph search based method was 7.71% higher on average than that of Hu's method(statistically significant, $p < 0.002$). Thus, from the sensitivity aspect, we could conclude for pathological lung CT data set the graph search based method is better than Hu's method.

Figure 3.16: Sensitivity analysis plot of graph search based method on 15 abnormal thorax CT data sets.

### 3.2.2   Segmentation Specificity

Specificity illustrates how effective of the segmentation algorithm when used on background pixels. The algorithm is perfect for background pixel detection if the specificity is 1, and random if the specific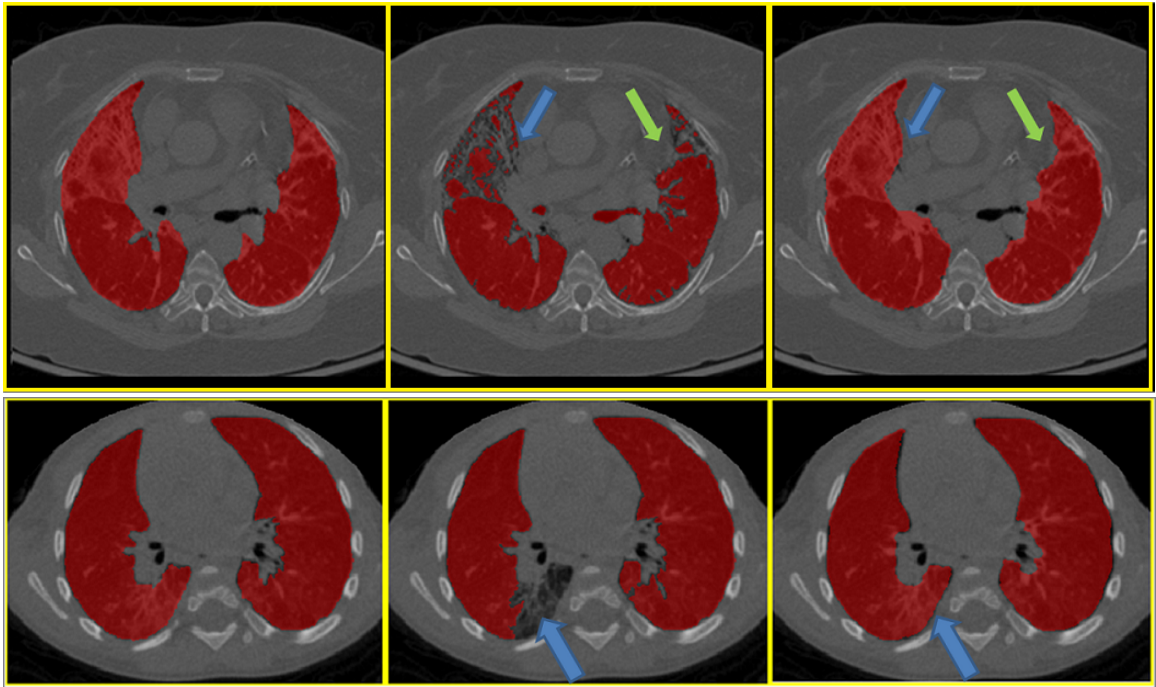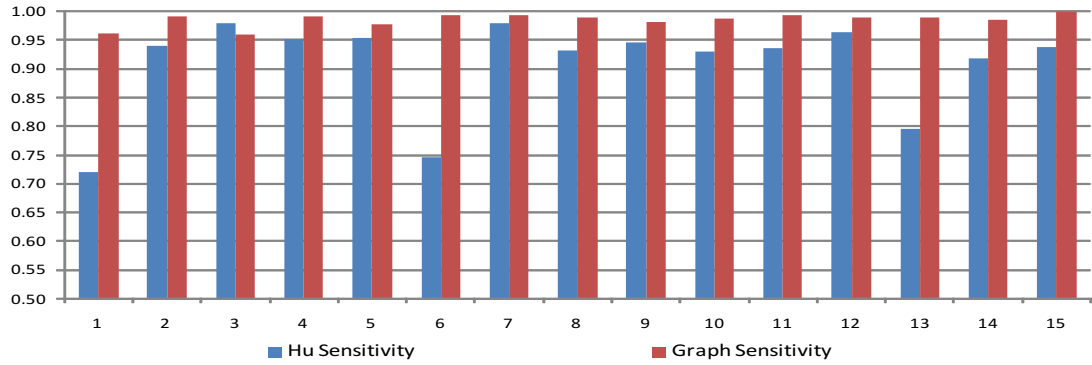ity is 0.5. The larger the specificity is, the better the segmentation result is. Figure 3.17 illustrates the specificity of 15 abnormal lung CT data sets using both the graph search based method results and Hu's method results with manual segmentation ground truth. In figure 3.17, the red bars represent the specificity of the graph search based method, while the blue bars represent the specificity of Hu's method. The blue bars have almost the same height as the red bars which means that for the graph search based method has similar specificity as Hu's method. Thus, from the specificity aspect, we could conclude Hu's method is more conservative than the graph search based method.

### 3.2.3   Boundary Position Accuracy

Since the lungs have large volumes, high volume overlap rate could not measure the small local boundary error. Hence, the Hausdorff distance between the manually-
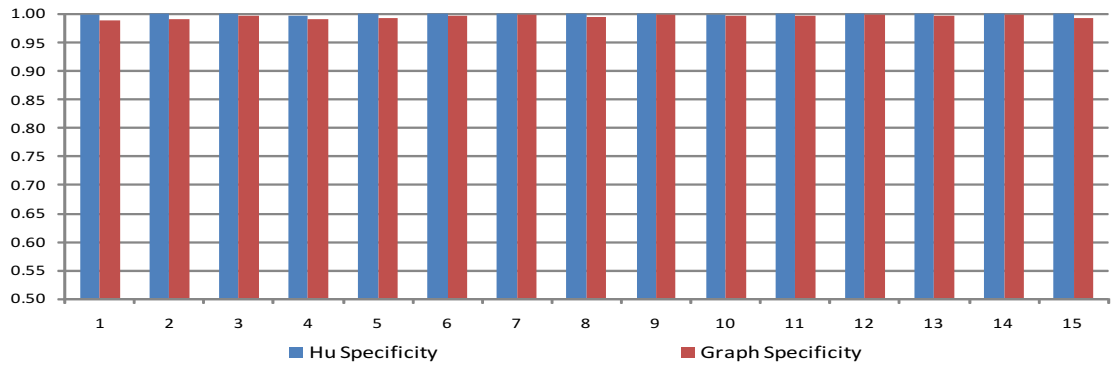
Figure 3.17: Specificity analysis plot of graph search based method on 15 abnormal thorax CT data sets.

defined lung boundaries and the computer-defined lung boundaries was used to access the border position accuracy. Hausdorff distance measures the largest surface distance between two contours by computing the distance between the set of non-zero voxels of two image contours. The algorithm is perfect for background pixel detection if the Hausdorff distance is 0. The smaller the Hausdorff distance is, the better the segmentation result is. Figure 3.18 illustrates the Hausdorff distance of 15 abnormal CT data sets using both the graph search based method results and Hu's method results with manual segmentation ground truth. The red bars represent the specificity of the graph search based method, while the blue bars represent the specificity of Hu's method. In figure 3.18, the blue bars are always shorter than the red bars which means that for pathological lung data set the graph search based method has a shorter Hausdorff distance than Hu's method. The table 3.6 shows the Hausdorff distance of the graph search based method was 16.8 pixels smaller on average than that of Hu's method(statistically significant, $p < 0.001$). Thus, from the Hausdorff distance aspect, we could conclude that the graph search based method is better than Hu's method.
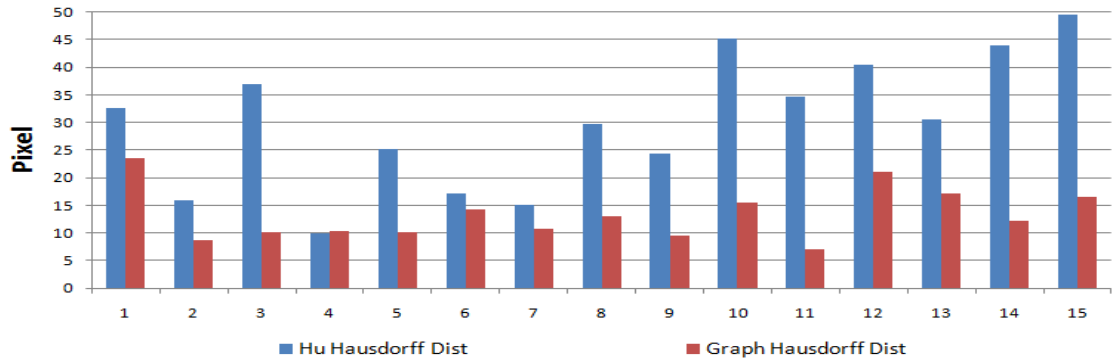
Figure 3.18: Hausdorff distance analysis plot of graph search based method on 15 abnormal thorax CT data sets.

| Method | Sensitivity | Specificity | Hausdorff Distance |
|---|---|---|---|
| $Hu's$ | $0.908 \pm 0.083$ | $0.999 \pm 0.001$ | $30.1 \pm 12.1$ |
| $GraphSearch$ | $0.986 \pm 0.011$ | $0.995 \pm 0.003$ | $13.3 \pm 4.7$ |

Table 3.6: Summary of graph search based method evaluation.

### 3.2.4 Efficiency

The graph search algorithm is an efficient approach to obtain a globally optimal segmentation surface that represent object boundary. It converts the segmentation problem into a maximum flow problem. The algorithm time complexity is low-order polynomial, is thus very efficient. The averaged running time of the graph search based method is around 5 minutes which is much faster than single threaded geodesic active contour based method, but similar to the multi-threaded geodesic active contour based method.

## 3.3   Results on Sheep CT data

The geodesic active contour method was also tested on the sheep CT data set. Figure 3.19 gives an example of sheep thorax CT data set segmentation result using

geodesic active contour combined with the registration result. Rigid and non-rigid registration based on the rib information were employ to register two rib cages. Step by step registration result is shown in Fig 3.20, 3.21, 3.22 . The transformation obtained from the registration was used to map the lung region of the template image to the moving image. The mapped lung region near the spine was combined with the geodesic active contour based method. Although the segmentation result is better compared with intensity only based method, We still have problem near the diaphragm.
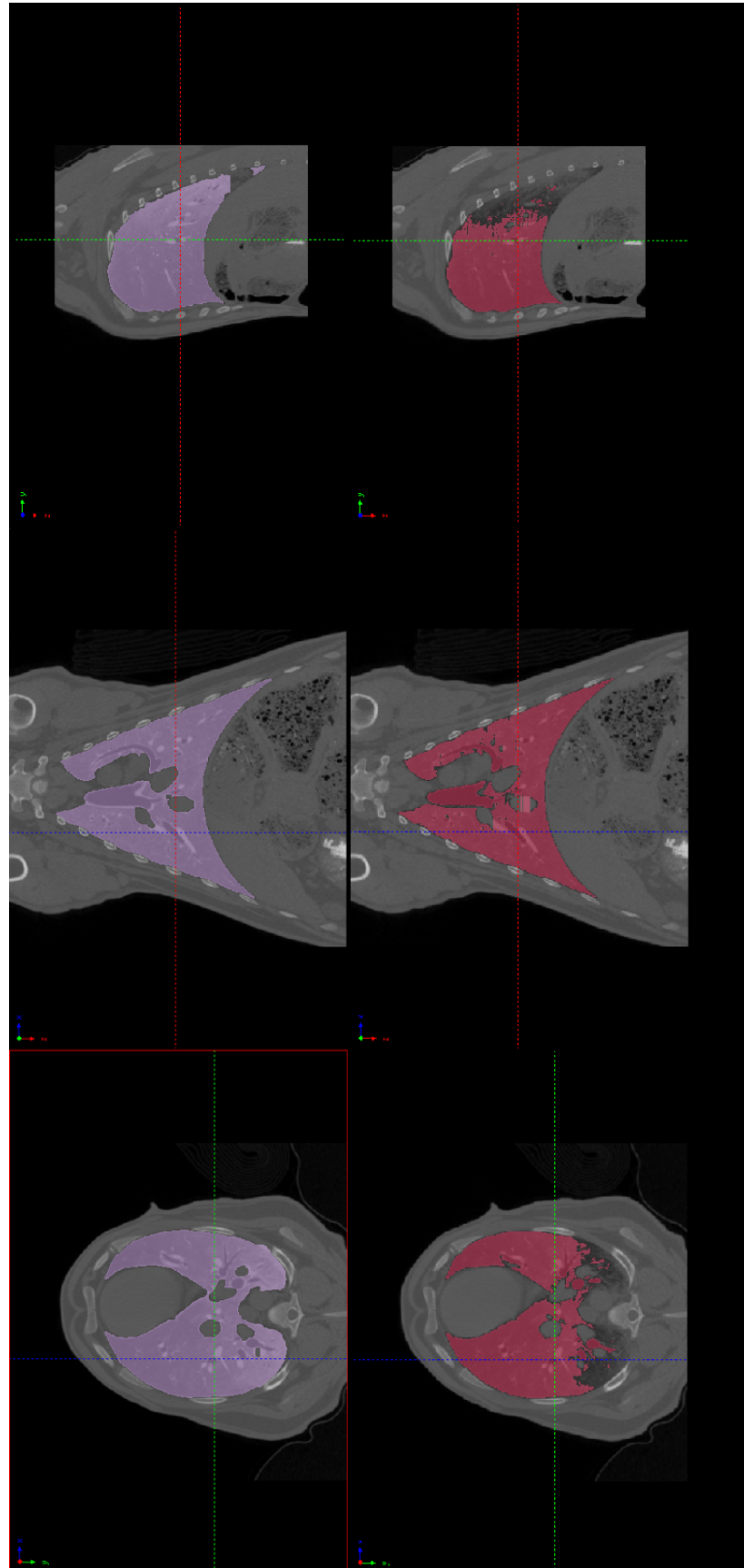
Figure 3.19: The segmentation result of one sheep thorax CT data set using geodesic active contour.

Figure 3.20: The overlap between ribs of two subjects before registration. The yellow region is the overlapped region. The red and green region are the non-overlapped region.

Figure 3.21: The overlap between ribs of two subjects after rigid registration. The yellow region is the overlapped region. The red and green region are the non-overlapped region.
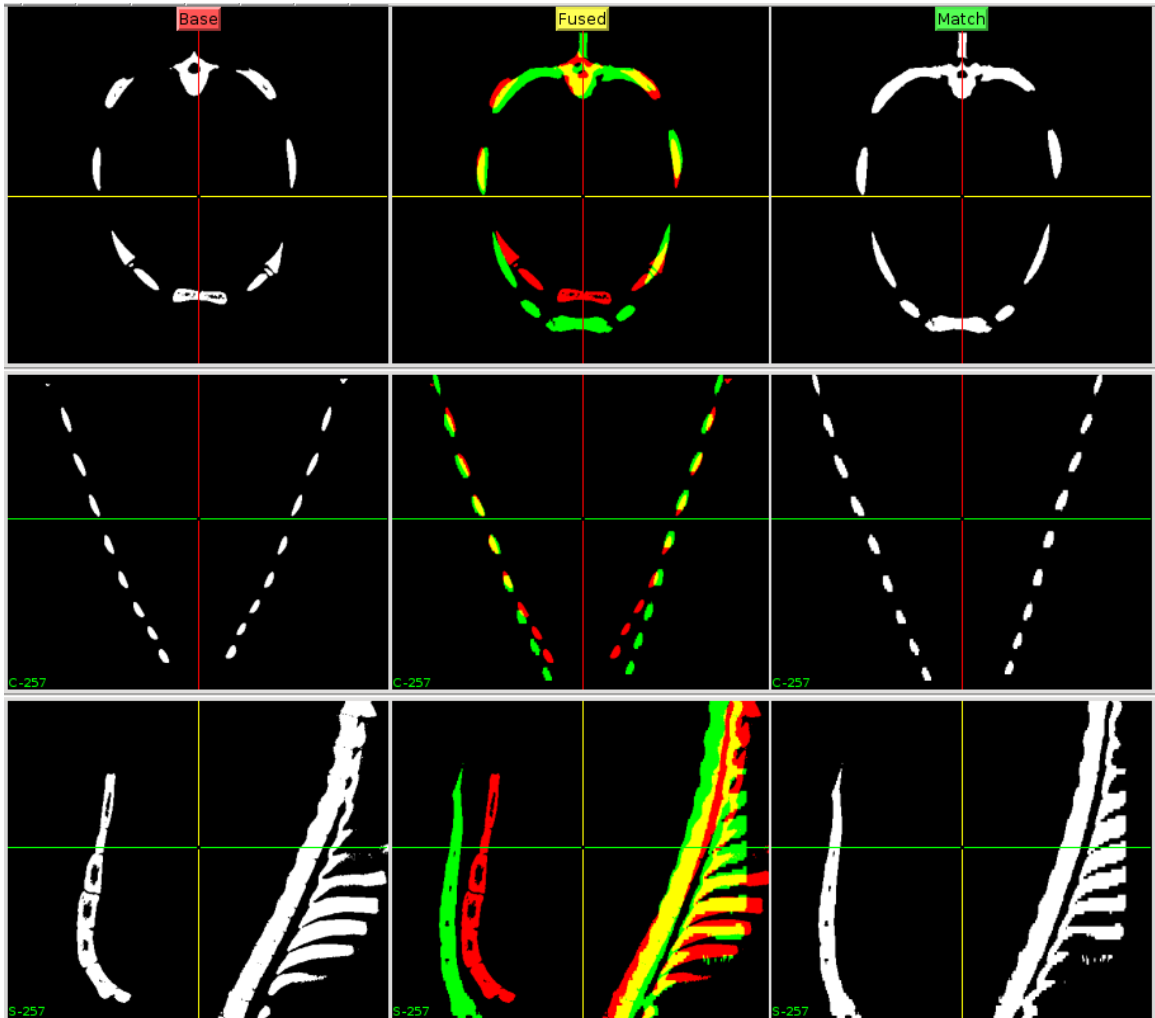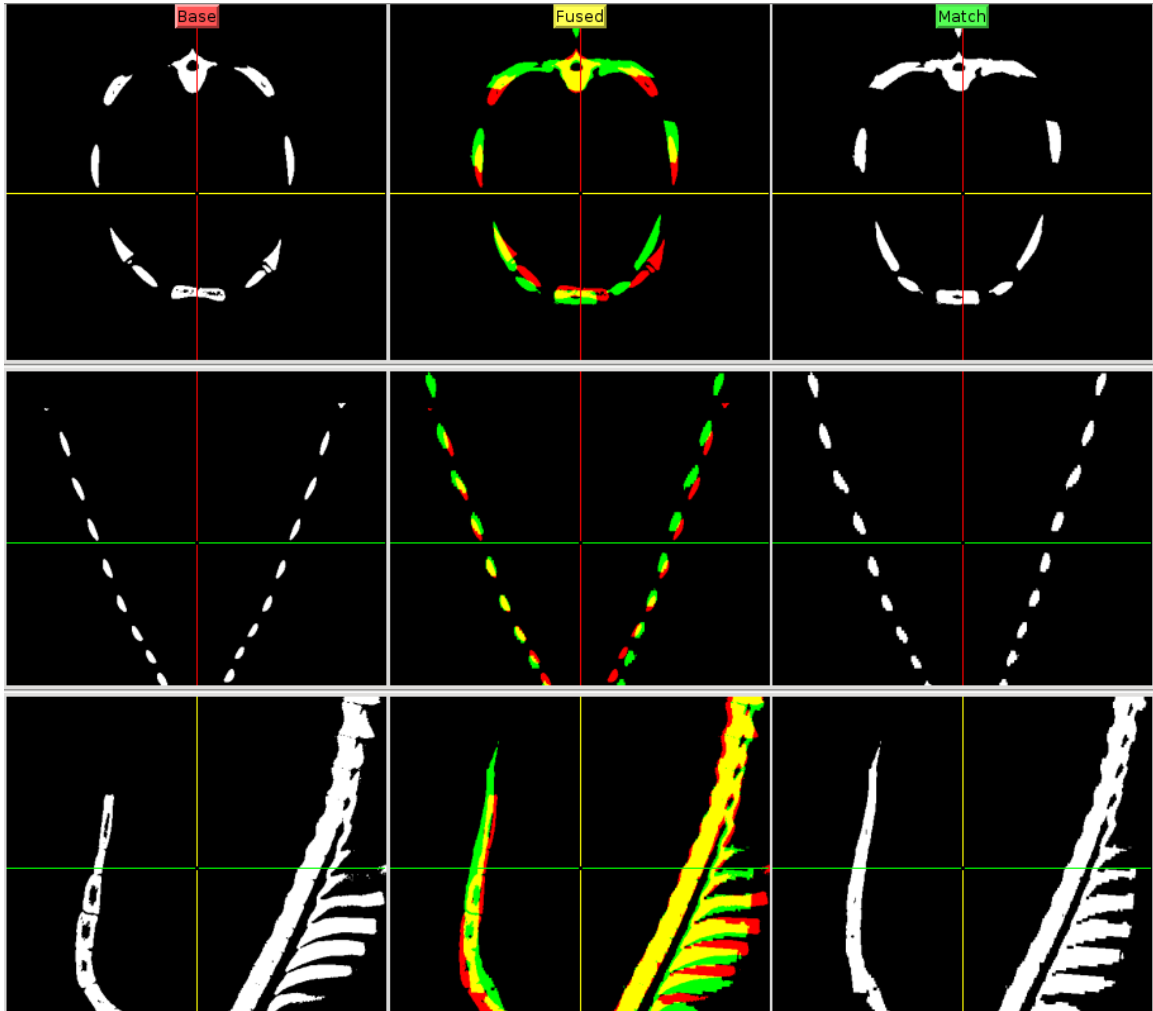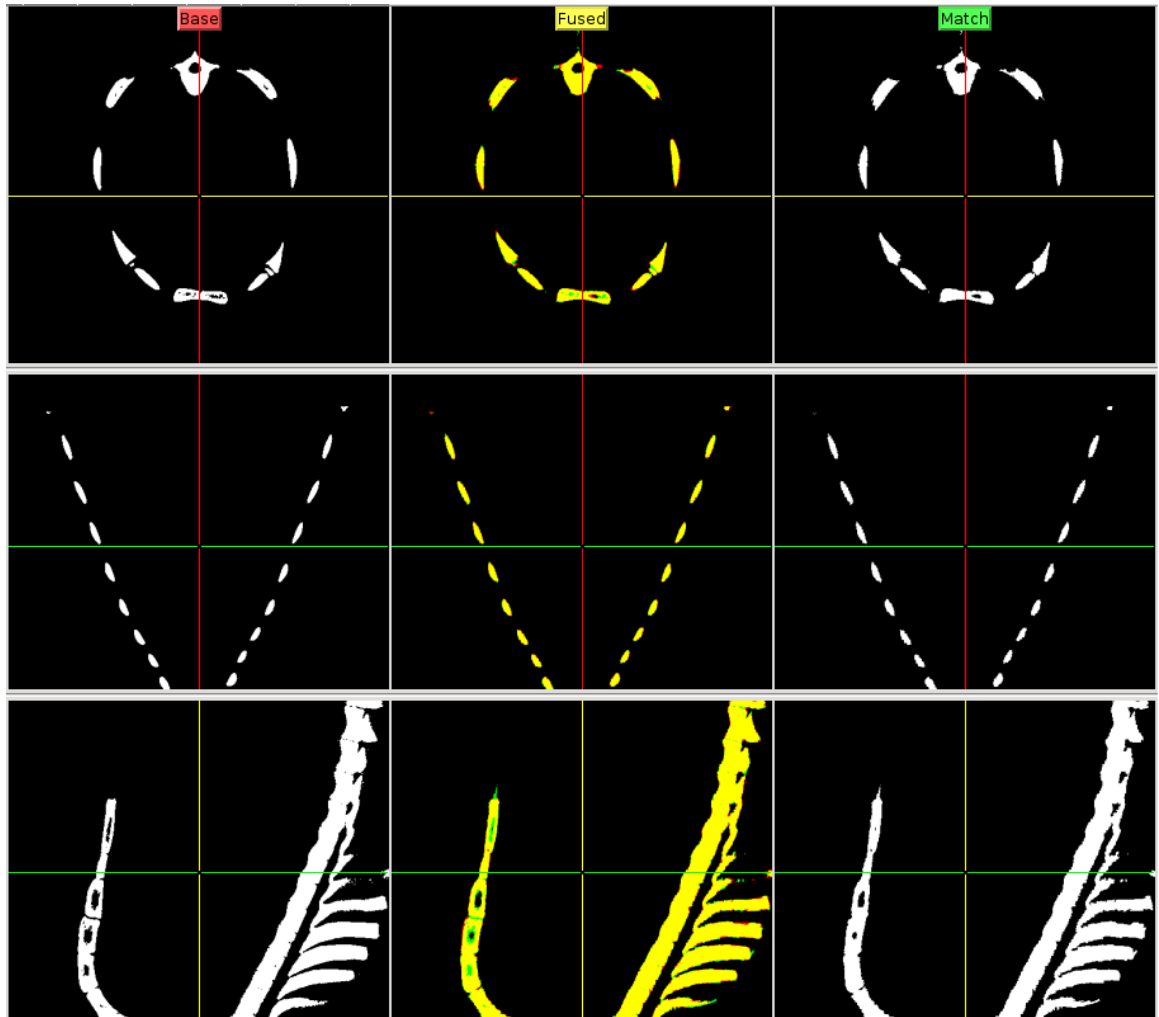
Figure 3.22: The overlap between ribs of two subjects after non-rigid registration. The yellow region is the overlapped region. The red and green region are the non-overlapped region. We can see from the aboving figure, the green and red region size reduces, almost every region is yellow which means an excellent rib registration.

**CHAPTER 4**
**DISCUSSION**

## 4.1   Geodesic Active Contour vs Graph Search

In this section, the geodesic active contour based method and the graph search based method are compared from the running time, sensitivity, specificity and Hausdorff distance aspects. Figure  4.1  4.2  4.3 show the comparison result between these two methods. From the sensitivity and specificity aspects, the geodesic active contour and the graph search algorithm are very similar. From the Hausdorff distance aspect, the graph search based method are a little better than the geodesic active contour method.



Figure 4.1: The sensitivity plot of the geodesic active contour based method and the graph search based method.

Figure 4.2: The specificity plot of the geodesic active contour based method and the graph search based method.



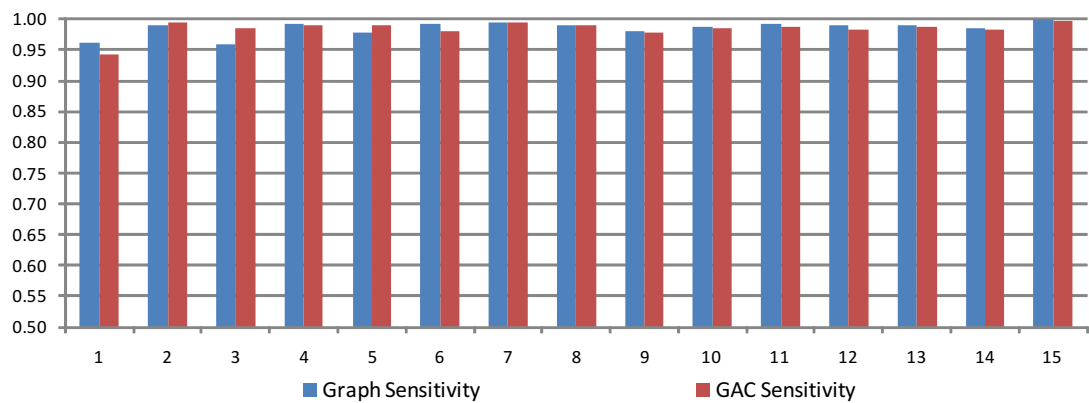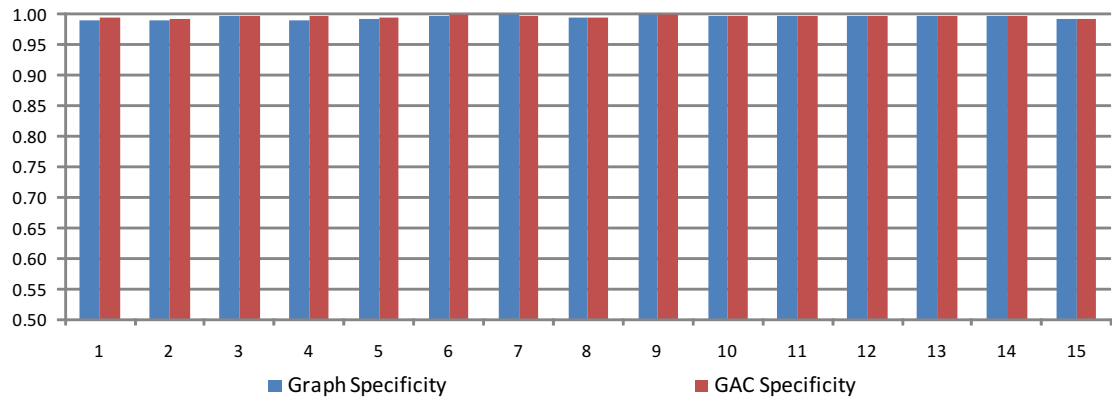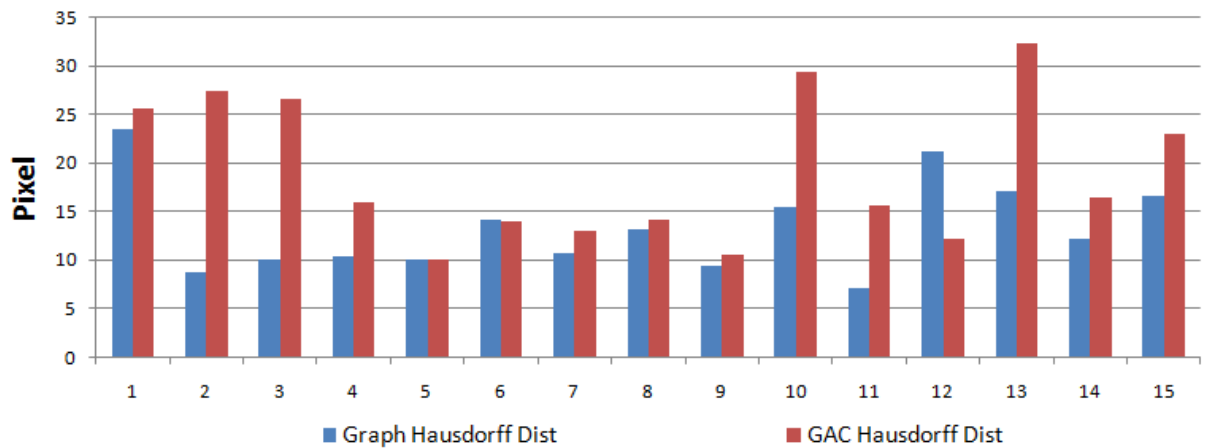Figure 4.3: The hausdorff distance plot of the geodesic active contour based method and the graph search based method.

## 4.2 Limitations and Future Improvements

Here, we tried to run the algorithm at three different scales simultaneously by using multi-threading to speed up the whole algorithm. The mean running time of the geodesic active contour method for one CT data set is around 5 minutes which is a little bit time consuming. P. Muyan-Ozcelik et al. [21] implement the Demons registration using the CUDA which speed up the registration ten times faster. It will be very helpful if we could use GPU programming (such as CUDA) to parallel the algorithms and to speed up the whole algorithm.

When the lung region has a large abnormal tissue near the diaphragm, both two segmentation algorithms might have problem with the region near the diaphragm. Because near the diaphragm, the lung bottom surfaces always change its shape with the contract of the diaphragm during different breathing phases. When segmenting the lung from the thorax CT images, we have no breath phase information or lung bottom surface shape information. It would be interesting if we could construct a 4D lung shape model to help the lung segmentation.

Moveover, it would be also interesting if we could use the rib and spine framework relative position information to detect the breath phase and then use the breath phase information to help the segmentation. During the inhalation phase, the diaphragm contracts, the ribcage expands and the contents of the abdomen are moved downward which will result the change of the lung bottom surface position and curvature. After the classifier are trained with large CT data sets to learn the breathing phase features, it will provide the phase information based on the initial lung segmentation, rib and spine detection result. Then in return, the breath phase information could help the lung segmentation. The phase detector could also help the lung disease

detection. For example, if there are large lung regions with very low intensity(below 900) in the FRC CT images, the subject are more likely to have emphysema. However, it would be a normal subject if the large low intensity lung region appears in the TLC CT images.

# CHAPTER 5
# CONCLUSION

We have described two algorithms that try to combine surrounding anatomical information, intensity, gradient, boundary smoothness to obtain an optimal segmentation for pathological lung region in thorax CT images. Geodesic Active contour and graph search algorithm are used to adjust the boundary to obtain an more accurate lung segmentation. We tested the geodesic active contour based method on 21 abnormal CT data sets and 32 normal CT data sets. We compare the segmentation result with Hu's method. For the 21 abnormal data sets, the sensitivity of the geodesic active contour is much higher than that of Hu's method. The specificity of the geodesic active contour method is similar as that of Hu's method. The Hausdorff distance of the geodesic active contour method is much smaller than that of Hu's method. For the 32 normal data sets, the sensitivity, specificity, and the Hausdorff distance of the geodesic active contour and Hu's method are very similar. Thus, for the abnormal thorax CT data set geodesic active contour have a better performance than Hu's method, while for the normal thorax CT data set geodesic active contour and Hu's method both performance very well. Moreover, the geodesic active contour based method could attain a more smooth cut between the airway/vessel and the lung region. Additionally, we trained the graph search cost function using 4 pathological lung CT data sets and tested on 15 pathological thorax CT data sets. The result is also compared with Hu's method, from the sensitivity and Hausdorff aspects, the graph search based method is much better than Hu's method. For the specificity, the graph search based method and Hu's method are similar. Hence, we conclude that

we developed two pathological lung segmentation algorithms which had a better performance than Hu's method for abnormal thorax CT data sets, such as emphysema, fibrosis, honey combing lungs.

# REFERENCES

[1] A.M. Ali, A.S. El-Baz, and A.A. Farag. A novel framework for accurate lung segmentation using graph cuts. *Biomedical Imaging: From Nano to Macro, 2007. ISBI 2007. 4th IEEE International Symposium on*, pages 908–911, Feb. 2007.

[2] S. G. Armato and M. L. Giger. Automated lung segmentation for thoracic CT. *Academic Radiology*, 11(9):1011–1021, Aug. 2004.

[3] Olegalexandrov at en.wikipedia. Level set method - wikipedia, the free encyclopedia. http://en.wikipedia.org/wiki/Level_set_method, (accessed by April 8 2010).

[4] H. Becker, W. Nettleton, P. Meyers, J. Sweeney, and Jr. C. Nice. Digital computer determination of a medical diagnostic index directly from chest x-ray images. *IEEE Trans. Biomed. Eng.*, BME(11):67–72, July 1964.

[5] M. S. Brown and M. F. McNitt-Gray. Method for segmenting chest CT image data using an anatomical model: preliminary results. *IEEE Trans. Med. Imag.*, 16(6):828–839, Dec. 1997.

[6] Matthew S. Brown and M. F. McNitt-Gray. Knowledge-based segmentation of thoracic computed tomography images for assessment of split lung function. *Med Phys.*, 27(3):592–598, Mar. 2000.

[7] V. Caselles, R. Kimmel, and G. Sapiro. Geodesic active contours. *International Journal of Computer Vision*, 22(1):61–79, July 1997.

[8] A El-Ba, G Gimel'farb, R Falk, T Holland, and T Shaffer. A new stochastic framework for accurate lung segmentation. *Med Image Comput Comput Assist Interv.*, 11(1):322–330, Feb. 2008.

[9] Youth Educate Health for Kids. Thorax anatomy. http://youtheducatehealthfor kids.org, (accessed by April 12 2010).

[10] Youth Educate Health for Kids. Human anatomy. http://youtheducatehealthfor kids.org/aboutus.aspx, (accessed by March 22 2010).

[11] M.K. Garvin, M.D. Abramoff, R. Kardon, S.R. Russell, X. Wu, and M. Sonka. Intraretinal layer segmentation of macular optical coherence tomography images using optimal 3-D graph search. *IEEE Trans. Med. Imag.*, 27(10):1495 – 1505, Oct. 2008.

[12] S. Hu, E.A. Hoffman, and J.M. Reinhardt. Automatic lung segmentation for accurate quantitation of volumetric x-ray CT images. *IEEE Trans. Med. Imag.*, 20:490–498, June 2001.

[13] W. A. Kalender, H. Fichte, W. Bautz, and M. Skalej. Semiautomatic evaluation procedures for quantitative CT of the lung. *J. Comput. Assist.Tomogr.*, 15(2):248–255, March 1991.

[14] G.J. Kemerink, R.J.S. Lamers, B.J. Pellis, H.H. Kruize, and J.M.A. Engelshoven. On segmentation of lung parenchyma in quantitative computed tomography of the lung. *Medical Physics*, 25(12):2432–2439, Dec. 1998.

[15] Kinecare. Physiotherapy and wellness rehabilitation clinic. http://www.kinecare .net, (accessed by March 8 2010).

[16] Jan-Martin Kuhnigk, Horst K. Hahn, Milo Hindennach, Volker Dicken, Stefan Krass, and Heinz-Otto Peitgen. Lung lobe segmentation by anatomy-guided 3d watershed transform. *Proc. of SPIE*, 4(23):1482–1490, Mar.-Apr. 2003.

[17] B. Li and J.M. Reinhardt. Automatic generation of 3-d shape models and their application to tomographic image segmentation. In *SPIE Med Imaging*, volume 4322, pages 311–322, 2001.

[18] K. Li, X. Wu, D.Z. Chen, and M. Sonka. Optimal surface segmentation in volumetric images - a graph-theoretic approach. *PAMI*, 28(1):119–134, Jan. 2006.

[19] R. Malladi, J.A. Sethian, and B.C. Vemuri. Shape modelling with front propagation: A level set approach. *IEEE Transactions On Pattern Analysis and Machine Intelligence*, 17(2):158–175, Feb. 1995.

[20] P. Meyers, Jr. C. Nice, H. Becker, W. Nettleton, J. Sweeney, and G. Meckstroth. Automated computer analysis of radiographic images. *Radiology*, 83:1029–1034, Dec. 1964.

[21] P. Muyan-Ozcelik, JD. Owens, J. Xia, and S.S. Samant. Fast deformable registration on the GPU: A CUDA implementation of demons. *Proceedings of 2008 ICCSA, IEEE Computer Society Press*, 32(6):452–462, June 2008.

[22] M. N. Prasad, M. S. Brown, S. Ahmada, F. Abtin, J. Allen, I. da Costa, H. J. Kim, M. F. McNitt-Graya, and J. G. Goldin. Automatic segmentation of lung parenchyma in the presence of diseases based on curvature of ribs. *Academic Radiology*, 15(9):1173–1180, Feb. 2008.

[23] J. Pu, J. Roos, C. Yi, S. Napel, G.D. Rubin, and D.S. Paik. Adaptive border marching algorithm: Automatic lung segmentation on chest CT images. *Comput Med Imaging Graph*, June 2008.

[24] Annual report 2008. American lung association. http://www.lungusa.org/associations/states/new-york/about/annual-report-2008.html, (accessed by April 5 2010).

[25] Graham Simpson. Thoracic computed tomography: principles and practice. *IEEE Trans. Med. Imag.*, 32(4):105C107, Sep. 2009.

[26] I. Sluimer, M. Prokop, and B. van Ginneken. Toward automated segmentation of the pathological lung in CT. *IEEE Trans. Med. Imag.*, 24(8):1025–1038, Aug. 2005.

[27] Q. Song, X. Wu, Y. Liu, M. Smith, J. Buatti, and M. Sonka. Simultaneous searching of globally optimal interacting surfaces with convex shape prior penalty. *CVPR*, pages 2879–2886, June 2010.

[28] Milan Sonka, Vaclav Hlavac, and Roger Boyle. *Image Processing, Analysis, and Machine Vision*, chapter 6.2.6. Thomson Learning, 2008.

[29] Omid Talakoub, Javad Alirezaie, and Paul Babyn. Lung segmentation in pulmonary CT images using wavelet transform. pages 453–456, 2007.

[30] B. van Ginneken, A.F. Frangi, J.J. Staal, B.M. ter Haar Romeny, and M.A. Viergever. Active shape model segmentation with optimal features. *IEEE Trans. Med. Imag.*, 21(8):924–933, Aug. 2002.

[31] E.M. van Rikxoort, B. de Hoop, M.A. Viergever, M. Prokop, and B. van Ginneken. Automatic lung segmentation from thoracic CT scans using a hybrid approach with error detection. *Medical Physics*, 36(7):2934–2947, July 2009.

[32] J. Wang, F. Li, and Q. Li. Automated segmentation of lungs with severe interstitial lung disease in CT. *Medical Physics*, 36(10):4592–4599, Oct. 2009.

[33] YassineMrabet. Sagittal plan - wikipedia, the free encyclopedia. http://en.wikipedia.org/wiki/Saggittal_plane, (accessed by April 2 2010).

[34] Y. Yin, Q. Song, and M. Sonka. Electric field theory motivated graph construction for optimal medical image segmentation. *Graph-Based Representations in Pattern Recognition*, 5534:334–342, July 2009.

[35] B. Zheng, J.K. Leader III, G.S. Maitz, B.E. Chapman, C.R. Fuhrman, R.M. Rogers, F.C. Sciurba, A. Perez, P. Thompson, W.F. Good, and D. Gur. A simple method for automated lung segmentation in x-ray CT images. In *Proc. SPIE*, volume 5032, page 1455, 2003.